

A Modeling Study of the Principal Rainband in Hurricane Matthew (2016) and the
Influence of Remote Terrain on Hurricane Structure During its Intensification in the
Southern Caribbean

Aaron Updike

Thesis submitted to the faculty of the Virginia Polytechnic Institute and State University
in partial fulfillment of the requirements for the degree of

Master of Science
In
Geography

Stephanie Zick, Chair
Andrew Ellis, Member
Yang Shao, Member

April 12th, 2019
Blacksburg, VA

Keywords: Tropical Cyclone, Terrain, Convection, Precipitation

A Modeling Study of the Principal Rainband in Hurricane Matthew (2016) and the Influence of Remote Terrain on Hurricane Structure During its Intensification in the Southern Caribbean

Aaron Updike

ABSTRACT

Hurricane Matthew (2016) was a category 5 hurricane that interacted with remote terrain over northern South America in the early stages of its life cycle. Because tropical cyclone (TC) precipitation and convection are known to be crucial factors in the understanding and forecasting of TC intensity, this study investigates how this terrain impacted Hurricane Matthew's rainband structure. Remote terrain is hypothesized to play a role in the strength of TC rainband convection by modifying the thermodynamic environment such that subsiding dry air advects over an extremely moist ocean surface layer leading to increased moist static instability. To investigate this hypothesis, this study utilizes the Advanced Research Weather and Research Forecasting Model (WRF-ARW) to create a high-resolution (2-km horizontal grid spacing) control simulation (CTL) of Hurricane Matthew and a second experimental simulation with a 50% reduction of terrain height over the topography of northern South America (T50). This study focuses on a particular convective rainband positioned downstream of the terrain that displayed prolonged robust convection during the initial stages of Hurricane Matthew's life cycle. Results indicate that characteristics of this robust rainband are consistent with prior research on an inner core rainband called a principal rainband. This rainband does not display differences in intensity in the two simulations but is located closer to the TC center and more persistent in the control simulation. In the region downstream of the topography, significantly ($p < 0.05$) drier conditions exist in the control simulation, which is consistent with the hypothesis that downslope motion would lead to a drier air mass. TC structural changes are also apparent, with a weaker TC in the reduced topography simulation. This research emphasizes the potentially important role of terrain distant from the TC center with possible influences on TC rainband convection and warm core structure. Conclusions of this research are limited due to the small sample size of a single case study. An ensemble modeling study and additional cases are needed for a more thorough conclusion on the impact of remote terrain on TC structure.

A Modeling Study of the Principal Rainband in Hurricane Matthew (2016) and the Influence of Remote Terrain on Hurricane Structure During its Intensification in the Southern Caribbean

Aaron Updike

GENERAL AUDIENCE ABSTRACT

Predicting the intensity of hurricanes remains a monumental challenge for hurricane forecasters. Many factors can influence the intensity of hurricanes, including the strength, frequency, and spatial distribution of hurricane rainbands (band of precipitation). The hypothesis for this study is that terrain distant from the hurricane center can alter the hurricane environment and cause more frequent and stronger rainbands to form. To assess this hypothesis, I use a weather model to simulate Hurricane Matthew (2016) while it was interacting with remote terrain over northern South America on September 30 - October 1, 2016. Then I use the same model, but with terrain height reduced by 50% over northern South America and analyze the similarities and differences in the hurricane structure and rainband patterns. The results of this study suggest that terrain did not alter the peak rain rates in the hurricane rainbands but may have caused more frequent, widespread, and prolonged precipitation. Also, differences in hurricane structure were apparent when comparing the two model simulations. The reduced terrain simulation produced a weaker hurricane, lending some evidence to support the hypothesis that terrain may have played a role in altering the hurricane structure. These results demonstrate the potential importance of distant terrain on forecasting hurricane precipitation and intensity.

ACKNOWLEDGEMENTS

First and foremost, I would like to thank my advisor Dr. Stephanie Zick for her guidance and mentorship over the last two years. Her continuous positivity and support provided the confidence needed to produce a quality research product and develop useful skills for future career endeavors. I couldn't ask for a better mentor during my experience as a graduate student.

Second, I would like to thank the rest of my committee, Dr. Andrew Ellis and Dr. Yang Shao, for providing a beacon of inspiration. You are both great role models in academia and I appreciate the beneficial lessons on communicating research. I would also like to thank the Virginia Tech Department of Geography for contributing a place to prosper and grow and for alleviating the financial burden of continuing my education. Within the department, I would also like to thank the graduate student cohort. They were the perfect colleagues to endure the process of finalizing a thesis.

Last, but certainly not least, I would like to thank my family and my fiancé for listening and providing words of encouragement during tough situations, and for always supporting me in my career aspirations. I can honestly say that I would not be where I am today without these wonderful individuals in my life.

Chapter 1: Introduction.....	1
Chapter 2: Review of Literature.....	5
2.1 Tropical Meteorology	
2.2 Tropical Cyclones	6
2.3 Wind Shear	
2.4 Tropical Cyclone Structure	7
2.5 Stationary Band Complex	9
2.6 Outer Mesoscale Convective Systems	12
2.7 Topographic Influences	
2.8 Hurricane Matthew	14
Chapter 2 Figures	17
Chapter 3: Methodology.....	21
3.1 WRF Model	
3.2 Model Configuration and Experimental Design	
3.3 Analysis of Principal Rainband in Control Simulation	22
Chapter 3 Figures	25
Chapter 3 Tables	26
Chapter 4: Control Simulation Results.....	27
4.1 Verification of Control Simulation	
4.2 Synoptic Environment and Precipitation Comparison	29
4.3 Observations and Parameters of the Principal Rainband	30
4.4 Summary of Control Simulation and Principal Rainband	31
Chapter 4 Figures	33
Chapter 5: Reduced Terrain Simulation Results.....	42
5.1 Synoptic and Inner Core Structure Observations	
5.2 Comparison of Reduced Terrain and Control Precipitation	44
5.3 Comparison of Reduced Terrain and Control Thermodynamics	46
5.4 Summary of Terrain Impacts on the PRB and TC Structure	49
Chapter 5 Figures	51
Chapter 5 Tables	66
Chapter 6: Conclusion and Future Work.....	69
References.....	72

Chapter 1

INTRODUCTION

Coastlines along the Atlantic Ocean, and more specifically the Caribbean Sea, are some of the premiere destinations for beach and water loving individuals. Nevertheless, all entities located in this region become highly aware of extreme weather during the months of June through November, otherwise known as the “hurricane season”. Over the last decade, the Atlantic basin has experienced 145 tropical storms (storms with sustained winds greater than 17 meters per second), and of those tropical storms, 28 have been categorized as major hurricanes with sustained winds greater than 50 meters per second. One major hurricane that caused damage in the Caribbean, and the focus of this study, was Hurricane Matthew in 2016. Peak wind gusts reported in Hurricane Matthew were in excess of 74 meters per second with greater than 500 millimeters of rain measured in some areas. Overall, 585 deaths were reported from the Lower Antilles to the coasts of the United States with the majority of deaths occurring in Haiti.

A tropical cyclone (TC) is a general term encompassing all rotating weather systems originating over tropical oceans. TCs can have various terminology associated with them, with regionally specific terms including “hurricane”. A hurricane is a tropical cyclone that originates in the Atlantic Ocean basin and has surpassed a wind threshold of 33 meters per second. The hazards of TCs and hurricanes have provided importance for their research with many research projects concentrating on TCs impact on coastal populations. Over the last few decades, TC structure has been a main focus of tropical meteorology research to better understand the inner core region, or the region with the lowest pressure and highest wind speeds encompassing the eye, eyewall, and connecting rainbands (Weatherford and Gray, 1988), due to the damaging precipitation and winds

found in this region. There are other components within TCs that cause significant damage, including principal rainbands (PRBs) and outer mesoscale convective systems (MCSs). Only a few studies have focused on the PRB, most notably Willoughby et al. (1984) and Riemer (2016). Given that Hurricane Matthew occurred in 2016, little research has been formally published on this particular storm and PRB, providing a gap in the field that needs to be studied.

My focus on Hurricane Matthew is related to the rainband identified between 0000 UTC 30 SEP 2016 and 0000 UTC 3 OCT 2016 on satellite imagery (Fig 1.1). This particular rainband was extensive with prolonged robust convection leading to total rainfall amounts of over 350 millimeters in some areas. Hurricane Matthew was also unique in its location in the southern Caribbean, close to South America's northern coast, while simultaneously categorized as a category 5 hurricane on the Saffir-Simpson scale. On the coast of northwestern South America, there is elevated topography within Hurricane Matthew's wind field. This unique location along with its abnormal convection provides an interesting case study for an experimental research design in which I can study the influence of South American topography on TC structure and rainbands. Although robust, the rainband of concern has not been formally researched to be categorized as an inner or outer core structure. Analysis to identify if this particular rainband can be classified as an inner core structure will help provide guidance to my research when studying the rainband. Once the identification of the rainband has been established, I will delve into the topographic effects on this convective rainband. Further analysis will be done to provide an understanding of the effects of terrain remote from the inner core on the inner core, and more broadly, on what variables lead to robust convection in TC inner core rainbands. This research can also be applied to forecasting

precipitation and TC intensification. Jiang and Ramirez (2013) identified that TC inner core rainbands have a large impact on the moisture budget and latent heat processes within the inner core. Latent heating inside the inner core can lead to a more efficient environment for TC intensification (Shubert and Hack, 1982). This research will provide insight into the prerequisites of robust inner core convection, which will help to improve TC intensification forecasts.

With this in mind, there are three formal research questions:

- 1) Is Hurricane Matthew's robust, persistent convective feature associated with a principal rainband?**
- 2) Did the terrain over northern South America lead to enhanced convection in the rainband? If so, how?**
- 3) Can terrain that is remote from a tropical cyclone center have an influence on the inner core structure?**

The impact of terrain remote from the TC inner core on its structure remains a void in current tropical meteorology research. Physical geography, such as distant topography in the Caribbean Sea, may be important in understanding the entirety of TC structure, and this research will investigate its importance. Answering these questions will provide the content necessary to further understand how remote terrain affects TC inner core and rainband structure and, therefore, any impacts on precipitation and TC intensification.

Chapter 1 Figures

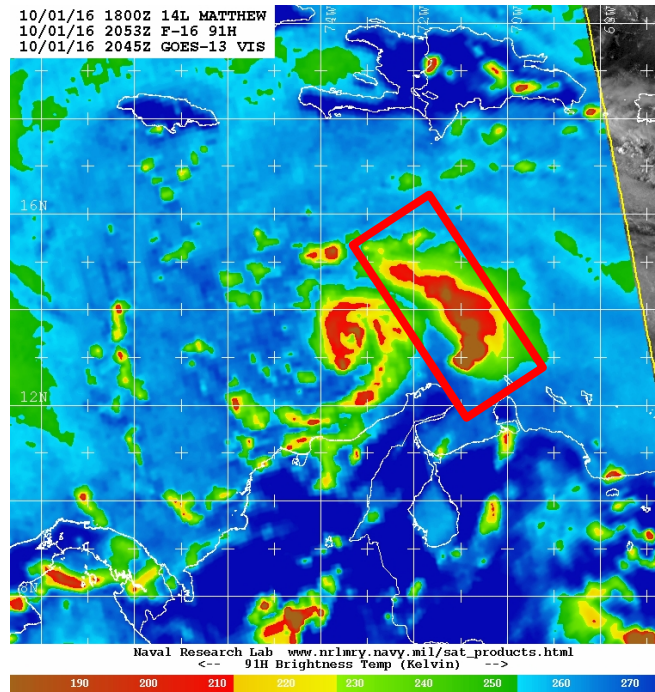


Figure 1.1: F16 91 GHz microwave satellite image of Hurricane Matthew, valid at 2053 UTC 01 October near peak intensity, just north of Columbia. The rainband of concern can be seen near (14°N, 71°W).

Chapter 2

REVIEW OF LITERATURE

2.1 Tropical Meteorology

Tropical meteorology is the sub-discipline of atmospheric science that concentrates on weather and climate in tropical regions, generally defined as the zone of convergence near the equator and between the subtropical highs found near 30 degrees north and south. The tropics can also be defined as the area between the Tropic of Cancer and the Tropic of Capricorn, or 23.5 degrees north and south respectively. The subsolar point lies between these two latitudes throughout the year, leading to enhanced incoming solar radiation in these regions in comparison to mid-latitude and polar regions. Due to the minimal variation of sun angle over this region, horizontal temperature and pressure gradients are weak, and due to a relatively low albedo and a low zenith angle, an excess of energy is absorbed in the tropics compared with mid-latitude and polar regions. Also, because of the rotational properties of the Earth, the Coriolis force is weak and approaches zero near the equator. Lastly, winds are predominantly out of the east in the tropics due to the trade winds created by the Hadley circulation. These characteristics create a vastly different atmosphere from the mid-latitudes (Liang and Evans, 2016). Within these tropical regions, TCs can develop. While rare, TCs have astonishing impacts on populous tropical regions leading them to be some of the most significant and extensively researched tropical systems. Although TCs have been heavily researched, new TCs occur every year providing additional research questions and data for exploring new and existing questions. Researching unique aspects and structures of TCs including Hurricane Matthew's convective feature is important to the broader understanding of TCs as a whole by further developing our knowledge on the physical connectivity of TC systems.

2.2 Tropical Cyclones

With the majority of Earth's solar radiation received in the tropics, energy transport is necessary to keep the atmosphere in balance. TCs are one form of energy transport from the tropics toward the poles. TCs occur in all three tropical oceans (Indian, Pacific, and Atlantic), and once specific criteria are met (generally, sustained winds greater than 33 meters per second), these tropical systems are called different names in each basin: cyclone, typhoon and hurricane, respectively. For this literature review, the main focus will be on the Atlantic Ocean basin and, thus, I will use the term "hurricane" interchangeably with TCs of winds > 33 meters per second. TC formation requires warm sea surface temperatures, usually greater than 26.5 degrees Celsius; weak upper level wind shear (defined in the next section); and an atmospheric disturbance poleward of approximately 5 degrees north or south in order to cause the convergence and rotation induced by the Coriolis force (Houze, 2010). Upon formation of a TC, easterlies within the tropical regions typically advect the system westward until it curves northward around the subtropical highs and moves into the mid-latitudes. Once in the mid-latitudes, tropical cyclones will weaken due to landfall or lower sea surface temperatures, and also typically undergo extratropical transition (ET) with an increase of baroclinicity and shear. (Jones et al. 2003; Houze, 2010)

2.3 Wind Shear

Wind shear is generally defined as the change in wind speed and/or direction over a distance. Shear can be contextualized in both the vertical and the horizontal dimensions. Wind shear is typically given a direction to better define the type of wind shear. For example, if the surface winds are stronger out of the west than winds aloft, then it would

be categorized as easterly shear because winds are becoming more easterly with height. In the Tropical Atlantic, vertical wind shear tends to be westerly or north-westerly, which has important implications for TC structure. Generally, vertical wind shear is detrimental to the formation and intensification of a TC, particularly when vertical wind shear exceeds 10 meters per second in the vicinity of the inner core (Gray 1968; Zehr 1992). However, weak to moderate vertical wind shear (5-10 meters per second, Frank and Ritchie 1999) can still impact TC structure. In more mature TCs, there is a larger resilience to vertical wind shear, due to the extent and magnitude of the radius of maximum winds and its resistance to further tilting of the TC inner core (Reasor et al. 2004; Wang and Holland, 1996). Vertical wind shear can also play a primary role in the formation of TC asymmetric structures (Bender 1997), which will be further discussed in the next section.

2.4 Tropical Cyclone Structure

Tropical cyclone structure can be described in a multitude of ways due to important physical processes across multiple spatial scales. On the smallest spatial scales, there are microphysical processes including latent heat release and development of precipitation. On the mesoscale, there are convective processes that collectively organize the convection, and on the synoptic scale, processes include the warm core low pressure system and its associated primary and secondary circulations. For this research, I will analyze a combination of mesoscale (convection) and synoptic-scale (winds) processes in Hurricane Matthew.

There are two main sections of a TC: the inner and outer core (Fig. 2.1). The inner core, which encompasses the eye, eyewall and inner rainbands, is imperative to its strength and life cycle because it is responsible for transporting energy from the ocean to

the atmosphere through latent heat release in the eyewall (Malkus and Riehl, 1958; Wang and Wu 2004). Within the eye, sinking motion is observed, causing the perceived “hole” in the TC center. The sinking motion inhibits convection (or cloud formation), which helps to explain the calm surface conditions experienced in the TC eye (Houze 2010). Meanwhile, the eyewall, which is the circular band of rain immediately adjacent to the eye, is responsible for the maximum winds in the entire TC. Eyewall processes can also account for the TC’s intensity variations through what is called the eyewall replacement cycle (Willoughby et al. 1982; Willoughby et al. 1988; Houze et al. 2007). Occasionally, as the TC intensifies, convection outside of the initial eyewall becomes organized and forms a secondary ring of precipitation. When eyewall replacement occurs, the first eyewall contracts inward and then is replaced by the secondary eyewall (Willoughby et al. 1982). This process initially weakens the TC, but once the process is complete, along with favorable environmental conditions, an intensification of the wind field is frequently observed (Wang and Wu, 2004). Although the eyewall’s appearance gives the perception of a typical convective cloud, it differs by an added component of horizontal accelerations due to inertial forces (Houze, 2010) which give the eyewall its highly circular structure.

A TC’s rainbands are also important in its overall structure. These rainbands can be split into two separate categories based on congruent parameters and radial distance from the center of the storm: inner rainbands and outer rainbands. The inner rainbands are located in the TC inner core, typically within a 150-km radius of the center, while the outer rainbands are typically found within a 150 to 500-km radius of the center (Wang and Wu, 2004; Weatherford and Gray, 1988; Jiang et al. 2013). Montgomery and Kallenbach (1997) described inner rainbands as being generated by vortex Rossby waves,

whereas the generation of outer rainbands remains in dispute (e.g., Li and Wang 2012, Cheng-Ku et al. 2018). The inner rainband region can have both symmetric and asymmetric tendencies, and similar to the eyewall, plays an important role in TC intensification (Willoughby et al. 1984). Both inner rainbands and outer rainbands have been associated with heavy rainfall and can produce hurricane force winds.

Assessing the overall structure of a TC is important to understanding precipitation patterns, but it is also important to recognize the convective properties in relation to wind shear. Corbosiero and Molinari (2003) performed an observational study analyzing the location of lightning strikes in relation to the vertical shear and the storm motion, both of which result in convective asymmetries. They found a concentration of lightning strikes within the outer core in the downshear right quadrant of the TC. They also found a concentration of lightning strikes in the downshear left quadrant associated with rainbands in the inner core. The Corbosiero and Molinari (2003) observational study corroborated research in idealized modeling environments explored in Frank and Ritchie (1999). Observations also indicate that the strength of the vertical wind shear is important in identifying clusters of lightning strikes (Corbosiero and Molinari, 2003). Weak vertical wind shear displays a more concentric layout of lightning strikes with a slight prevalence on the downshear side of the tropical cyclone, whereas in a strong shear environment, the lightning strikes appear strongly asymmetric with a strong prevalence on the downshear side.

2.5 Stationary Band Complex

Explanations behind symmetric versus asymmetric inner core structures have been widely researched. In idealized simulations with little to no vertical wind shear, the inner core of a TC can have symmetric tendencies for prolonged periods (Emanuel, 1988);

however, in observations, asymmetric or oblong inner cores are more prevalent. Asymmetries can occur in different forms and are frequently quantified given a wavenumber. For example, wavenumber one asymmetries have one maximum and minimum value encircling the TC. Asymmetric processes may also be necessary for rapid intensification (Nolan et al. 2007; Braun et al. 2006). Multiple hypotheses have attempted to explain why asymmetry occurs. Wang and Wu (2004) concurred with Guinn and Schubert's (1993) theory that asymmetric structures can occur due to imbalances in heat and moisture fluxes. Bender (1997) theorized that asymmetries mainly arise as a result of vertical wind shear. Vertical wind shear induced asymmetries are theorized to be due to the wavenumber one asymmetries in the eyewall structure within the low-level convergence field causing a forced vertical circulation to develop in order to restore balance (Frank and Ritchie 1999). Asymmetries are important to the understanding of TC intensification as some severe TCs have reached their maximum potential intensity through asymmetric processes within their inner core (Braun et al. 2006).

One type of asymmetric structure identified by Willoughby et al. (1984) is the stationary band complex (Fig. 2.2), described as “a group of prominent spiral bands that maintains a fixed position relative to the vortex” (Willoughby et al. 1984). Because the complex is stationary, inertial waves in which only kinetic energy is observed) are not present (Willoughby et al. 1984). The stationary band complex has three main components: the principal rainband (PRB), connecting band, and secondary bands. All three are perceived as quasi-stationary due to continuous up-shear convective development. Thus, these rainbands can produce prolonged rainfall over one area. The connecting band is a rainband that attaches the primary rainband to the eyewall (Willoughby et al. 1984). Convection can occur within the connecting band, but

stratiform clouds and precipitation are more likely. In some scenarios, the connecting band can erode due to dry air intrusion. The secondary bands are smaller and less prominent than the PRB; however, they are similar in that they are spiral-shaped and convective in nature. These secondary bands usually occur on the concave (inward) side of the PRB (Willoughby et al. 1984). The last component of the stationary band complex is the PRB, which is a curved convective band that occurs on the edge of the stationary band complex, extending outward from the eyewall (Willoughby et al. 1984). The convection within the PRB is caused through low-level convergence (Riemer 2016) and develops a circulation of sinking motion on the outer edge and rising motion on the inner edge of the rainband (Didlake and Houze, 2009). A portion of the outward edge of the PRB can occur in the outer core of the TC, and if present, displays stratiform precipitation characteristics of outer rainbands (Hence and Houze 2008).

A stationary band complex forms in most hurricanes and is usually found to be more compact in TCs in dry environments and more expansive in TCs in moist environments (Hill and Lackmann 2009, Ying and Zhang 2012). Ying and Zhang (2012) found that large scale moisture plays a major role in inner core structure by impeding (dry) or enhancing (moist) the outer core rainbands. The location of the stationary band complex is variable, but when present, it develops approximately at the interface between the inner and outer core where the Rossby number, a ratio between inertial and Coriolis forces, is near one (Willoughby et al. 1984). Riemer (2016) concluded that the stationary band complex forms due to vertical wind shear in response to tilting of the TC vortex. Convection within the stationary band complex is initiated through low level convergence (Corbosiero and Molinari, 2002; Hence and Houze, 2008; Riemer 2016). Compared with? Willoughby et al.'s (1984) proposed model of a typical stationary band

complex (Fig. 3), Riemer (2016) found similar results, but established that the dividing streamlines south of the vortex as well as the orientation of the asymmetric structure are determined by the westerly shear (Fig. 3). Riemer (2016) later concluded that the location of the deflection zone would change based upon the orientation of the vertical shear

2.6 Outer Mesoscale Convective Systems

In the outer rainband region, outer mesoscale convective systems (MCSs) can form >150 km from the eye and produce heavy rainfall (Lee et al. 2012, Chen et al. 2014). Whereas the stationary band complex and associated PRB are viewed as features of the inner core of the TC, outer MCSs are found in the outer core region (Lee et al. 2012). The PRB is associated with regions of predominantly convective based precipitation, dissimilar to outer MCSs, which consist mostly of stratiform precipitation (Willoughby et al. 1984, Chen et al. 2014). Most documentations of outer MCSs are focused on TCs in the North Pacific (Lee et al. 2012), where the TC outer circulation encounters elevated topography. Chen et al. (2014) found that terrain had an influence in the moisture budget of Typhoon Fengshen, creating a north to south moisture band. This band, along with interaction with monsoonal flow led to the formation of a long-lived outer MCS (Chen et al. 2016).

2.7 Topographic Influences

Hurricane Matthew's unique track into the southern Caribbean, and therefore its closer proximity to the South American terrain, may have influenced its thermodynamic environment and convective structure (Fig. 2.4). Few studies have examined how distant topography can influence the TC wind field and rainband structure. In two studies, Chen et al. (2014, 2016) categorized outer core MCSs into four different subtypes by their

differences in location and synoptic precipitation controls. They found that the monsoonal flow, along with the location of the TC wind field had the largest influence on the development of outer core MCSs. Terrain was found to be a component of initiation in southern outer core MCSs. Although, Chen et al. (2014) found that topography only accounted for 35 percent of the developed outer core MCSs.

The majority of TC research related to topography is focused on changes in storm intensity and track due to interaction with terrain, particularly in the Taiwan region. Based on theory and observations, weakening of the TC surface pressure and winds is thought to occur while the inner core passes over high terrain (Chang 1982; Ramsay and Leslie, 2008). Although there are few studies on TC rainband interaction with remote terrain, many studies have investigated the topographic effects on precipitation during landfall, more specifically during interactions with high terrain on islands. Bender et al. (1987) looked at multiple TCs intersecting and directly interacting with scattered island terrain by using a numerical modeling framework. They found that terrain induced downslope flow and led to a drier air mass within the TC circulation, causing a gradual weakening of TC intensity.

Remote terrain could alternatively promote TC precipitation as follows. In the lee of mountain ranges, an unstable atmosphere can form when cool dry air is transported downward through mechanical processes and subsequently advects over a moist surface (Houze 1993; Kovacs and Kirshbaum, 2016). This situation would lead to an air mass with warm, moist marine air overlaid by drier air, or a thermodynamic environment with enhanced convective instability. Convective instability is a state of the atmosphere where equivalent potential temperature, a thermodynamic quantity to determine the value where entropy is conserved moist adiabatically, decreases with height (lapse rate). When

referring to saturated air parcels under the same environmental conditions, the layer can be described as moist statically unstable. An environment that is moist statically unstable is favorable to convective development and thunderstorms. A similar thermodynamic environment is frequently observed over terrestrial surfaces in the central and southeastern United States (McNulty, 1995). Though this process is more typically observed to the east of the Rocky Mountains, it can be conceptualized for the convective environment in the southern Caribbean Sea when winds are out of the south moving over the northern highlands of Venezuela toward the Caribbean Sea (Fig. 2.3).

2.8 Hurricane Matthew

In this case study, I examine the effects of topography on the PRB in Hurricane Matthew, which formed from an easterly wave off the west coast of Africa on 23 September 2016. Over the next four days, it traveled westward as a tropical disturbance. Later, at 1200 UTC 28 September, the first recordings of surface wind speeds at tropical storm intensity were measured northwest of Barbados. With a large ridge to the north, Matthew continued its trek westward, strengthening over the warm waters of the southern Caribbean Sea. Between 1800 UTC 29 September and 0000 UTC 1 October, Hurricane Matthew underwent rapid intensification, escalating to its peak winds at 74 meters per second just north of Colombia. Its location of peak intensity made it the southernmost Category 5 hurricane (sustained wind speeds > 70 meters per second) in recorded history in the Atlantic basin (Stewart, 2017).

While in the southern Caribbean Sea, a robust convective rainband was noted to the east of the hurricane center. This rainband caused heavy precipitation over many of the southern Caribbean islands, including Curacao and Aruba. After the storm reached its

peak intensity, the ridge to its north weakened, and Hurricane Matthew turned north while weakening. Early reports state that weakening likely occurred due to a drop in sea surface temperature, most likely due to upwelling beneath the storm along the northern coast of South America. Eventually, Matthew made landfall on the southwest tip of Haiti at 1800 UTC 4 October. Continuing northward, Matthew impacted Cuba and the Bahamas before traveling along and just to the east of Florida's Atlantic coastline. Later in Matthew's life cycle, the cyclone made landfall as a Category 1 hurricane at a location just south of McClellanville, South Carolina. Lastly, Matthew underwent extratropical transition as it interacted with a mid-latitude low pressure system where last reports of tropical characteristics were documented on 11 October (Stewart, 2017).

Hurricane Matthew provides a unique case study for developing a better understanding of TC rainbands due to the vigorous convection that occurred between 0000 UTC 30 September 2016 and 0000 UTC 3 October 2016 in the southern Caribbean. The rainband's close proximity to the eye creates a research objective to verify if this particular rainband can be classified as a PRB within the stationary band complex. Further, the storm's location in the southern Caribbean Sea provides an opportunity to test the hypothesis that terrain over northern South America influenced the vertical moisture distribution to enhance the convection.

A better understanding on the impact of terrain on TC convection and structure will help improve TC precipitation and intensity forecasts. The hypothesis for this research is that terrain distant from the TC inner core modifies the atmospheric conditions leeward of the topography influencing the intensity and rate of TC rainband convection. Accurately forecasting precipitation amounts and duration remains an important caveat to public preparedness and is a vital justification for this research. Also,

due to the important role that inner core convection plays in TC intensification, improved understanding of the underlying physical mechanisms leading to robust convection in the inner core will lead to improved TC intensity forecasts.

Chapter 2 Figures

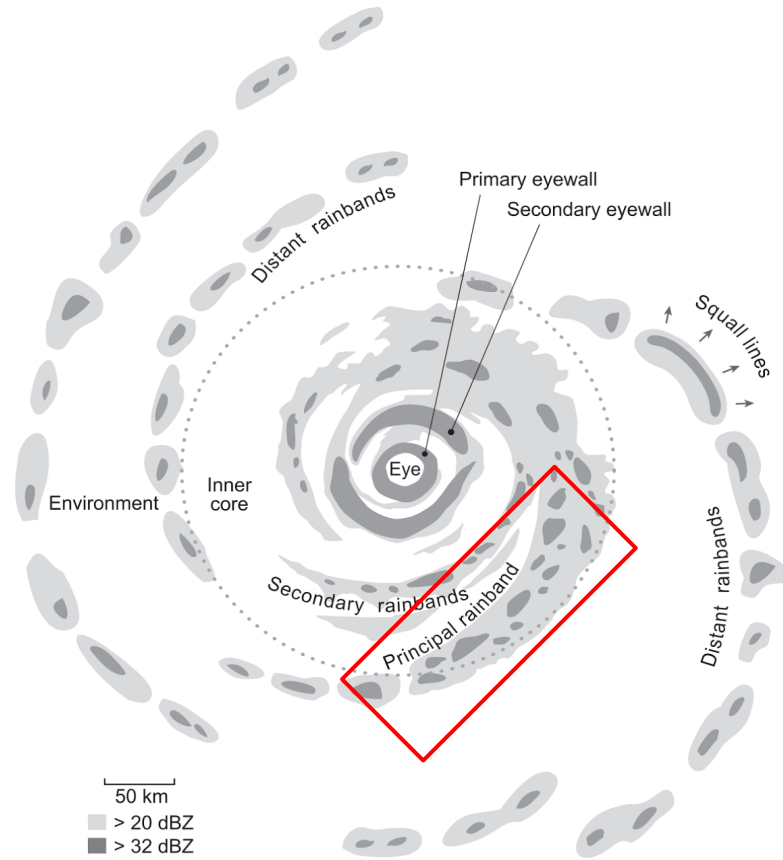


Figure 2.1: Precipitation bands in a mature tropical cyclone, adapted from Houze (2010). The red box delineates the principle rainband.

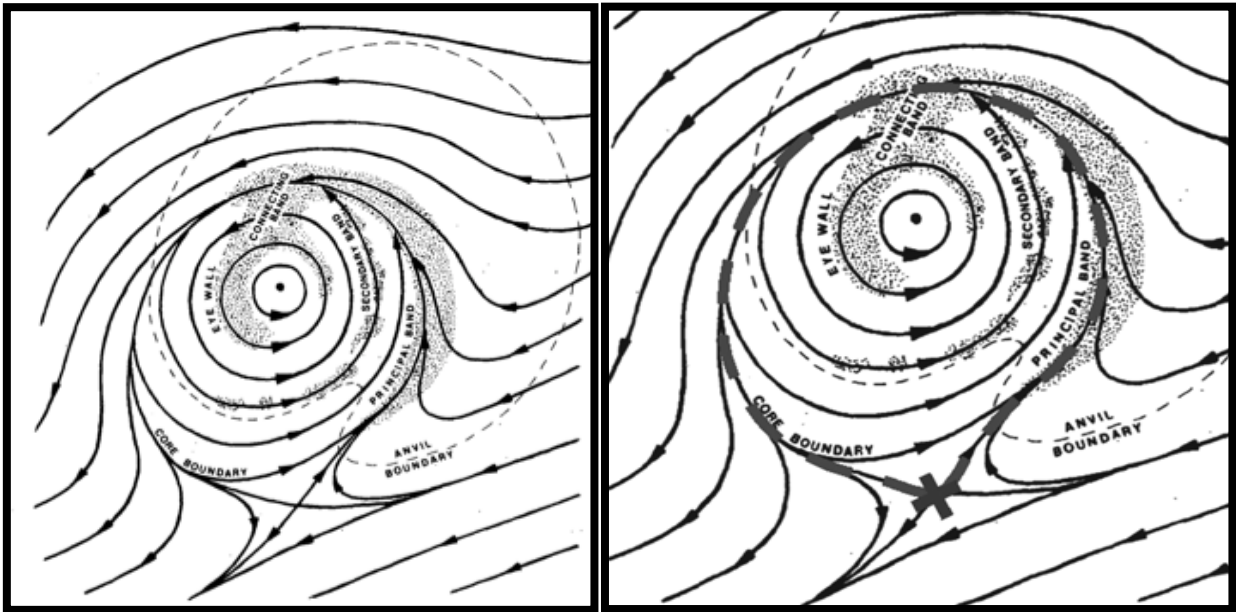


Figure 2.2: Riemer (2016) schematic of the stationary band complex streamlines (Right) based off of Willoughby et al. (1984) (Left). Both representations are exactly the same; however, Riemer (2016) indicates that based on the vertical wind shear direction, the orientation of the inner core asymmetries (thick dashed lines) and location of the deflection zone (cross) can be altered.

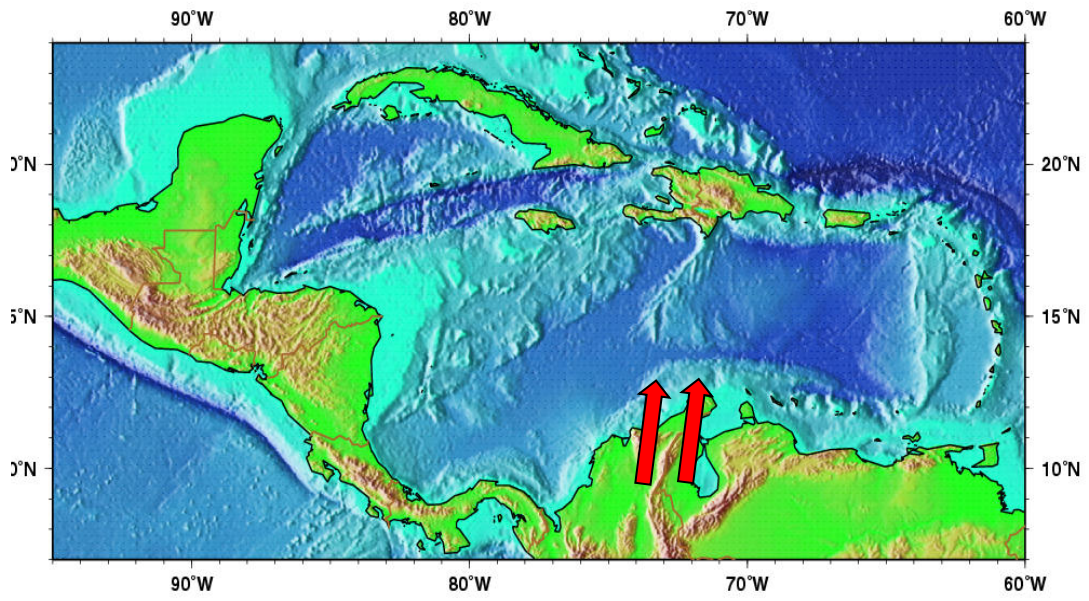


Figure 2.3: A conceptual illustration of south, south westerly winds over the terrain of northern South American that would lead to an enhanced environment for convective initiation

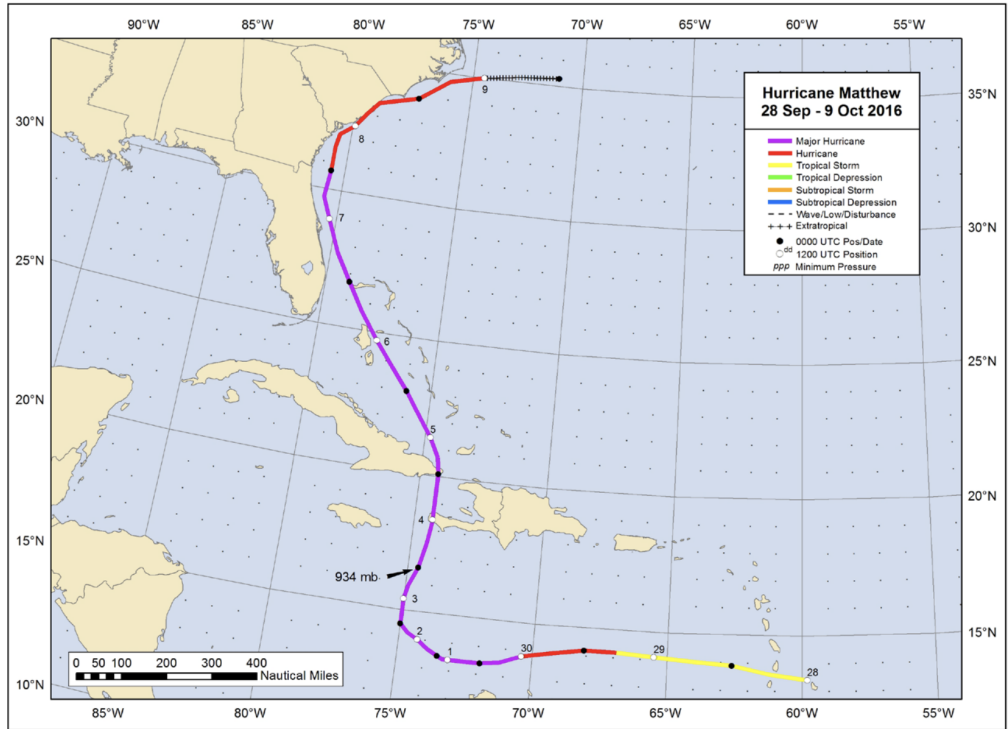


Figure 2.4: Observed best track of tropical cyclone Matthew’s lowest pressure in 12-hour increments from September 28th through October 9th, 2016 provided by the Hurricane Matthew Tropical Cyclone Report (Stewart, 2017). The best track visualizes the low latitudinal position of Hurricane Matthew during rapid intensification as well as the eventual minimum pressure recorded of 934 mb on October 3rd, 2016.

Chapter 3

METHODOLOGY

3.1 WRF Model

Within meteorology research and forecasting, numerical weather prediction (NWP) is utilized to simulate atmospheric conditions using mathematical algorithms supplied by initial atmospheric observations and conditions. For this research, I use the Advanced Research Weather Research and Forecasting (WRF-ARW) model version 3.6.1 (Skamarock et al. 2008). The WRF was developed as a collaboration across multiple organizations to lead an effort in advancing weather forecasting and research. The WRF-ARW is an open-source model with code written and updated by members of the WRF community. The Mesoscale and Microscale Meteorology (MMM) division of the National Center for Atmospheric Research (NCAR) provides the WRF community with training and documentation, freely available on their website (<http://www2.mmm.ucar.edu/wrf/users/>). The MMM also maintains and distributes the WRF software. The WRF-ARW dynamic core solves the non-hydrostatic Euler equations following a sigma vertical grid on an Arakawa-Cartesian (Arakawa-C) horizontal grid (see Arakawa and Lamb 1977). Time is integrated using a second or third order Runge-Kutta scheme (Skamarock et al. 2008).

3.2 Model Configuration and Experimental Design

In this study, I first analyze a control simulation (CTL) of Hurricane Matthew as the storm underwent rapid intensification and reached peak intensity in the southern Caribbean Sea. All simulations are performed using a two-way interactive nested grid

design (Fig. 3.1), with a coarse domain of 18-km horizontal resolution and nests of 6-km and 2 km, respectively. The 18-km outer domain is designed to capture the large-scale wind field in the Caribbean Sea as well as the trade wind easterlies in the equatorial region. All domains are initialized at 0000 UTC on 30 September 2016 with a Mercator grid centered at 14°N and 72.0°W (Fig. 3.1). Initial and boundary conditions are obtained from the Global Forecast System (GFS) final analysis, which is 0.25° horizontal resolution. Daily 0.5° real-time global (RTG) sea surface temperature (SST) data are interpolated to 6-hourly and provided for the lower boundary condition over the ocean. Upper level data are interpolated to a sigma following coordinate system with 40 vertical levels and a model top of 20 millibars. Because a 2-km grid spacing is unable to resolve smaller-scale physical processes, such as air-sea fluxes in the boundary layer and cloud microphysical processes, I utilize a set of physical parameterizations (Table 3.1) that are commonly employed in real simulations of TCs. Although model simulations of TCs are known to be sensitive to physical parameterizations (e.g., Davis and Bosart 2002), I do not account for these sensitivities in the current experimental design.

3.3 Analysis of Principal Rainband in Control Simulation

Before an altered simulation can be run, an assessment on the control simulation of the perceived PRB must be done to determine if the rainband's properties match the description of previous studies on PRBs. To do this, I will survey the low-level convergence (850 millibars) in correspondence with the heaviest precipitation of the rainband. This is in alignment with Willoughby (1984) and Riemer (2016) studies indicating convergence in the low-level wind field associated with the PRB. Environmental inertial stability can also be used to determine the location of the inner core. Inertial stability is largest in locations where the Coriolis and pressure gradient

forces are in balance and are more likely to return to balance when disturbed by external forces. This has been found to be true within the TC inner core, where tangential wind accelerations are the greatest (Schubert and Hack, 1982). I will use this framework to examine the inertial stability of the region to evaluate whether the rainband is within the inner core.

For the experimental design, I examine the high terrain over northern South America as it is hypothesized to play an important role in the anomalous convection. To examine this variable, I construct an experimental model simulation with elevation in northern South America reduced by 50 percent (T50). To assess the importance of terrain in the vicinity of Hurricane Matthew, I will compare the evolution of the simulated TCs in the control and experimental simulations. Impacts on track and intensity will first be examined by comparing the best track, maximum sustained winds and minimum mean sea level pressure of each experimental simulation to the control simulation. A comparison of 3-hour rainfall accumulation will also be performed to provide brief inclination as to how the altered simulations affected rainband convection. These processes will provide clarity to the holistic alterations of Hurricane Matthew. Next, a more thorough analysis of changes to the size and dynamic-convective structure will be performed by examining atmospheric motion, reflectivity and thermodynamic profiles. As the PRB is an asymmetric feature of the TC, I will also focus specifically on dynamic and thermodynamics structure of this rainband in the control and experimental simulations. To examine the differences in the inner core structure, I will create cross sections of azimuthally averaged tangential and radial winds and temperature anomalies. Any contrast in convection intensity and frequency between the two simulations is explained through thermodynamic profiles by analyzing the differences of temperature

and dewpoint temperature in the low-levels. Analysis of moist static stability is also conducted through equivalent potential temperature cross sections and lapse rates. A breakdown of the precipitation pattern will also be executed to distinguish any spatial differences in inner core structure. This will provide a better understanding of the changes in intensity of Hurricane Matthew and the role of inner core convection in the intensification process.

Chapter 3 Figures

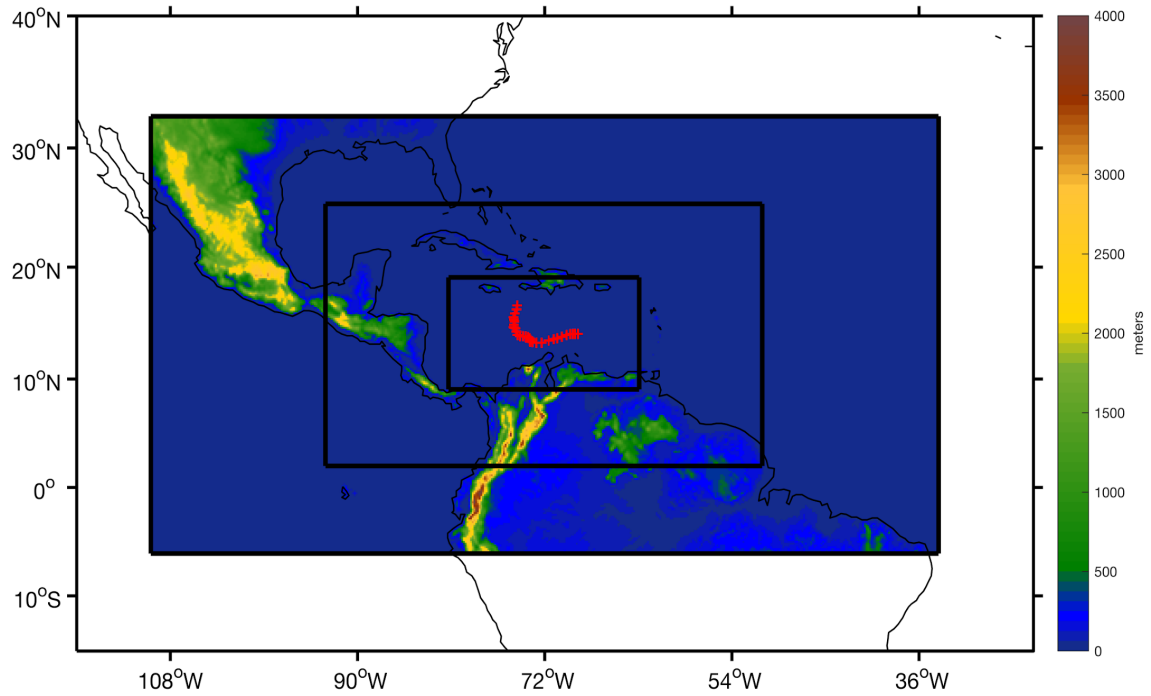


Figure 3.1: Model domain configuration for coarse domain and two nested grids (18, 6, and 2-km horizontal resolution) and terrain height (in meters) on the 18-km domain. Best track positions for Hurricane Matthew are overlaid for the observational times that coincide with all model simulations which begin 0000 UTC 30 Sept 2016 and end 0000 UTC 3 Oct 2016.

Chapter 3 Tables

Table 3.1: Physical parameterization schemes for all model simulations in analyzing the control simulation, where I concentrate on comparing the track, intensity, and structure of the simulated TC to observational data (Fig. 5, 6, 7).

Physical Parameterization	WRF-ARW v. 3.6.1 Option
Cumulus	Kain-Fritsch (18-km domain only)
Microphysics	WRF single-moment 6-class (WSM6)
Longwave Radiation	Rapid Radiative Transfer Model
Shortwave Radiation	Rapid Radiative Transfer Model
Planetary Boundary Layer	Yonsei University
Surface Layer	Revised MM5 surface layer scheme based on Monin-Obukohov similarity theory with a namelist flag to modify turbulent exchange coefficients over water during strong winds

Chapter 4

CONTROL SIMULATION RESULTS

For this study, a control experiment (CTL) is utilized to simulate Hurricane Matthew beginning at 00 UTC 30 September and ending at 00 UTC 3 October, a period that covers the early life cycle of Hurricane Matthew as it underwent RI and developed a persistent convective rainband northeast of the TC center. In this chapter, I aim to address the first research objective regarding the characterization of a rainband with persistent convection to the northeast of Hurricane Matthew's center. Prior to addressing this research question, it is necessary to first evaluate whether the CTL simulation adequately represents Hurricane Matthew to answer the major research questions proposed in Chapter 1. To do this, I compare model output to observations. In section 4.1, TC track and intensity are analyzed, followed by an assessment of the synoptic environment in section 4.2 to explain any differences between the model and observed. Differences between the CTL simulation and observations will help with understanding the experimental simulation in Chapter 5. Lastly, in Section 4.3 I delve into the specifics of the persistent convective rainband to determine if the rainband is within the TC inner core and its structure is consistent with a PRB.

4.1 Verification of CTL

In order to verify the performance of control simulations, best track positions and intensity are analyzed and compared. Here, I determine the TC center by locating the location of minimum mean sea-level pressure ($MSLP_{min}$) in the high resolution 2-km CTL simulation. The TC track plot (Fig. 4.1) indicates that the CTL simulation is initialized slightly to the northwest of the observed position at 00 UTC 30 September, by

a distance of approximately 0.25° latitude. This initial position difference is minimal, considering that the resolution of the GFS analysis used to initialize the model is also 0.25° latitude-longitude. Subsequently, a north bias in the track of the CTL TC persists throughout the rest of the simulation.

Comparison of the CTL and observed TC tracks also shows a difference in speed, with the distance between 6 hourly positions increasing during the beginning of the simulation. At 18 hours after initialization, when the CTL TC center is located at approximately 74°W , its position is approximately 12 hours ahead of the observed best track position. This difference in translation velocity still locates the TC near the South American coastline and should have minimal impact on the interaction between the terrain and the TC. Even so, these position differences need to be taken into account when comparing the CTL simulation to observed conditions.

Modeled and observed TC intensity are also compared to analyze the CTL. TC intensity in the CTL is determined using maximum sustained winds (MSW) at 10 meters and MSLP_{\min} at 3-hour intervals. Both the MSLP_{\min} (Fig. 4.2) and the 10-meter MSW (Fig. 4.3) show a similar TC strength at initiation with slight strengthening in the early timesteps. However, from 12 UTC to 21 UTC 30 September, the observed TC undergoes rapid intensification (RI) whereas the CTL only strengthens by approximately 5 millibars. Following this time period, both simulations weaken, which I will investigate in the next section. Because RI is difficult to capture, even in high-resolution models (Li and Pu, 2008; Pasrez-Betancourt, 2011), and because the overall intensity trend (increasing vs. decreasing) is consistent with observations, I conclude that the CTL simulation provides an adequate representation of TC intensity. Further, this conclusion is bolstered by similarities in TC rainband structure, which I discuss in section 4.2. Lastly, it is worth

nothing that there is a difference in geographic location of the TC center during this observed RI, which may contribute to the underestimation of intensity.

4.2 Synoptic Environment and Precipitation Comparison

Identifying and comparing key TC structural features and patterns can also be used to verify models against observations. For this specific study, TC rainbands, and therefore precipitation totals, are an important feature in verifying the CTL. Reflectivity can be difficult to verify in TC case studies given the scarcity of radar data over open ocean. With this in mind, satellite-derived rain rates are used to compare TC rainband location and intensity. Observed precipitation measurements are acquired from NASA's Global Precipitation Measuring (GPM) mission's Integration of Multiple-satellitE Retrievals from GPM (IMERG) dataset, which estimates precipitation using microwave and infrared satellite data, along with precipitation gauge measurements (Huffman et al. 2018). The values, derived at 30-minute intervals, are instantaneous and converted to hourly rain rates. At 12 UTC 01 October, the highest rainfall values are located northeast of the TC center (Fig. 4.4). This same pattern is observed in the CTL 3-hr precipitation totals at 00 UTC 01 October (Fig. 4.5). Due to the faster translation velocity of the modeled TC, similar rainfall observations in the CTL are seen 12 hours earlier than in the IMERG precipitation plots. This comparison, along with reflectivity from the CTL (Fig. 4.6), verifies that the CTL produced an approximate rainband with similar location and intensity to the observed rainband of concern.

The final step in verification is to analyze the environmental influences on the CTL. Differences in the synoptic scale environment can help explain track and intensity discrepancies described in section 4.1. Reasons for intensity differences can be difficult to pinpoint since an accurate forecast of intensity requires representation of small-scale

eyewall processes (Bryan and Rotunno, 2008; Gentry and Lackman, 2010; Davis, 2018). However, alterations in TC track can be directly related to the steering flow. In this instance, the observed steering flow just after CTL initialization at 00 UTC 30 September has a slightly smaller southerly component than the steering flow in the CTL (Fig. 4.7). An east-northeast steering flow along with northerly drifting due to latitudinal differences in the Coriolis force (beta drift), cause a westward TC track. A slightly reduced northerly component would cause the TC to track farther north due to beta drift. Also, the magnitude of the steering flow in the CTL simulation is around 5 knots stronger than the observed steering flow, which would support an accelerated TC track in the CTL. This pattern continues throughout the majority of Matthew's early life cycle (Fig. 4.8), explaining the slightly northern and accelerated TC track in the CTL.

4.3 Observations and Parameters of PRB

The first question tasked for this study is to distinguish whether or not this specific rainband (Fig 1.1) represents an inner or outer core feature. The PRB, in particular, is known to be found on the periphery of the inner core with strong convergence on the inner (upshear) edge of the convection (Willoughby et al. 1984, Corbosiero and Molinari, 2002; Hince and Houze, 2008; Reimer 2016). When looking at low-level convergence in association with the rainband (Fig. 4.5), the largest areas of convergence can be identified in this upshear portion of the convective band. Low level wind vectors at this time step (Fig. 4.5) also depict a similar location of convergence. This convergence of the low-level winds upshear of the strong precipitation amounts (NE of the TC center), indicates that this particular rainband is near the periphery of the inner core and fits previous studies on PRB features (Reimer, 2016).

A second, more quantitative approach can be used to locate the extent of the inner core through assessment of inertial stability. Within the inner core, inertial stability is high (see section 3.3). Thus, the PRB can be identified as a nearly stationary convective band at the periphery of regions of high inertial stability. To distinguish between the inner and outer core, previous studies have used inertial stability thresholds of 2 to $4 \times 10^{-7} \text{ s}^{-2}$ (Euler et al. 2018). As seen in Fig. 4.6, at 00 UTC October 1, the rainband is separated from the concentric region of larger inertial stability yet still exhibits values within the 2 to $4 \times 10^{-7} (\text{s}^{-2})$ range utilized in previous research.

Finally, I employ one additional diagnostic approach to evaluate whether the rainband structure is consistent with a PRB, which displays a specific vertical wind and reflectivity profile as noted in Hense and Houze (2008) and Didlake and Houze (2009). The vertical wind and reflectivity cross section at 00 UTC on 1 October in the CTL is shown in Fig. 4.7. This plot shows a slight area of descending air on the outward edge of the convective band with rapidly ascending air on the inner edge. This overturning circulation is found in most PRBs.

4.4 Summary of CTL Simulation and PRB

Overall, the CTL simulation produced an adequate representation of Hurricane Matthew to be used as a baseline for comparisons with the experimental simulation in chapter 5. The largest differences between the two simulations were 1) the lack of RI and 2) a faster translation speed shortly after initialization. Even with these differences, the CTL simulation produced meaningful and comparable output between 12 UTC 30 September and 12 UTC 01 October to analyze the PRB. During this time period, intensity, track, and precipitation patterns remained similar. The differences between the CTL and observed TC track are less than average NHC forecast guidance errors at 24

hours (40 n mi), 48 hours (50 n mi), and 72 hours (80 n mi) (Congialosi, 2018), which highlights the quality of the CTL simulation. Also during this time period, the CTL simulation produced a similar persistent convective feature northeast of the TC center. The rainband of concern was positioned within a region of inertial stability greater than 2 to $4 \times 10^{-7} \text{ s}^{-2}$, along with convergence on its inner side. Cross sectional analysis also depicted a circulation seen with most PRBs. Based on these parameters and observations, this convective feature displays characteristics of a PRB and can be considered a PRB for this study. With this conclusion, any variations in the rainband due to changes of topography in the experimental simulation will be closely analyzed in Ch. 5 to understand the effects on the TC rainbands and inner core.

Chapter 4 Figures

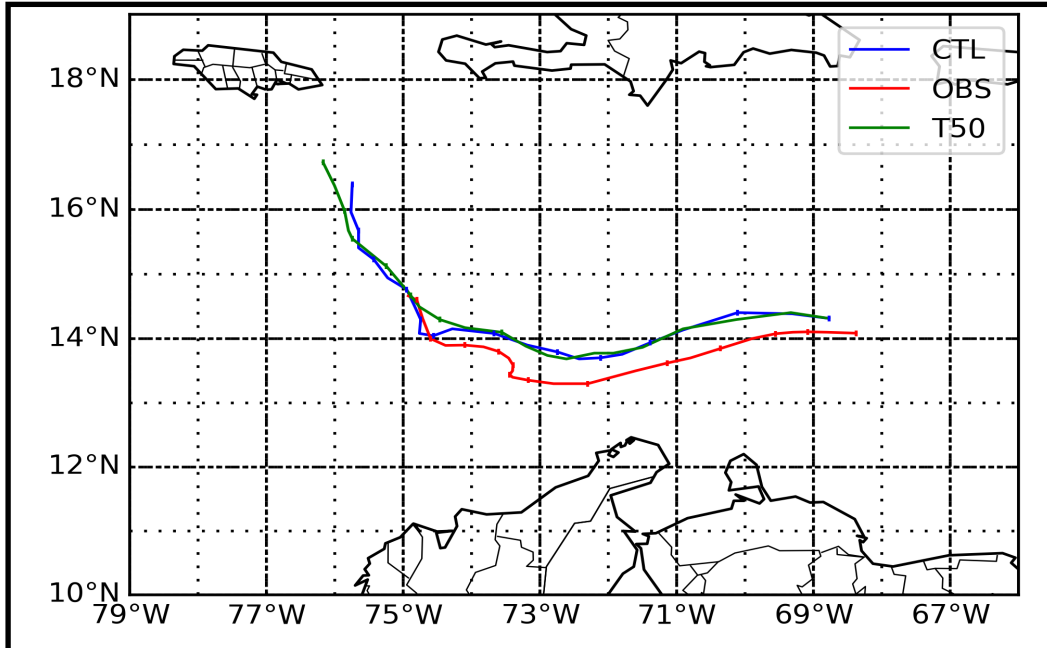


Figure 4.1: Comparison of best track position (OBS) and location of minimum mean sea level pressure in 2-km control (CTL) simulation and 2-km reduced terrain (T50) simulations. Tick marks are positioned at 6-hour intervals beginning at 00 UTC 30 September.

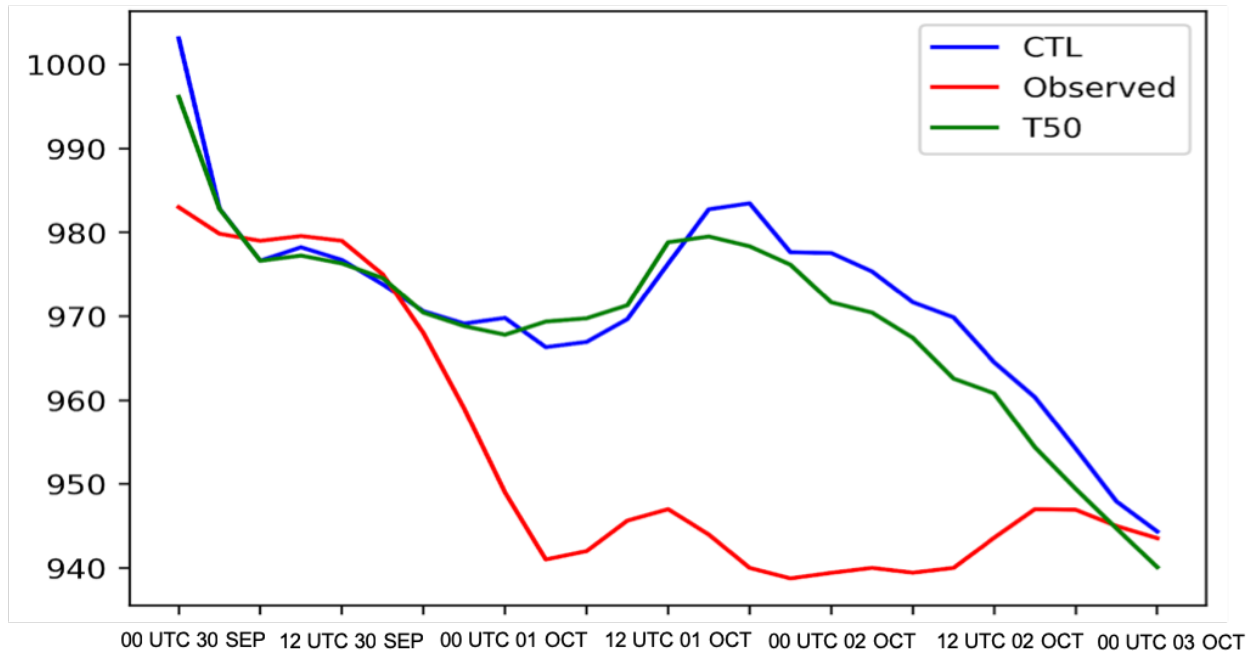


Figure 4.2: Comparison of minimum mean sea level pressure (hPa) in observations (Observed) and 2-km control (CTL) and reduced terrain simulation (T50) simulations from the beginning of the simulations at 00 UTC 30 September to the end of the simulations at 00 UTC 3 October.

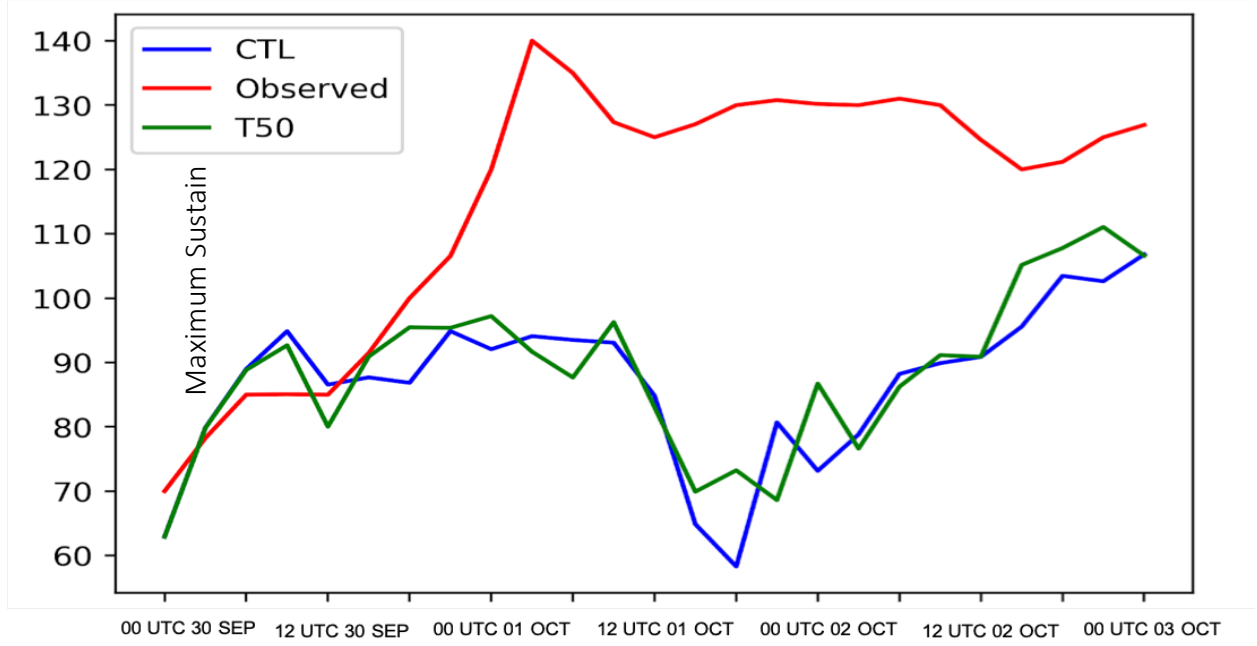


Figure 4.3: As in Fig. 4.2 but for 10-m maximum sustained winds (m/s).

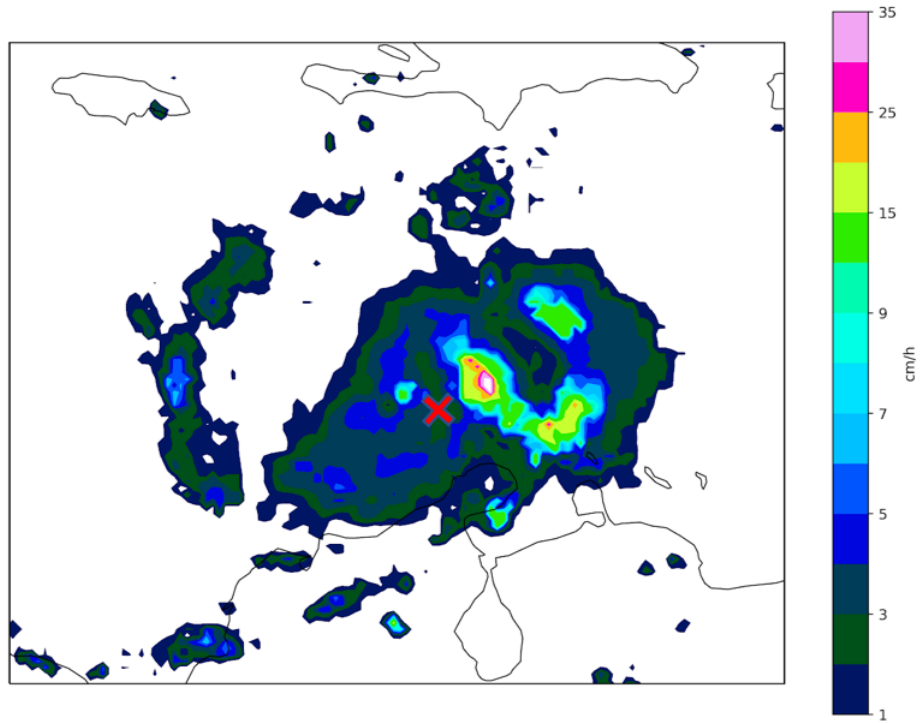


Figure 4.4: Instantaneous hourly rain rate at 1200 UTC on 01 October 2016 obtained from NASA's GPM IMERG database. Approximate center of TC is marked with a red X.

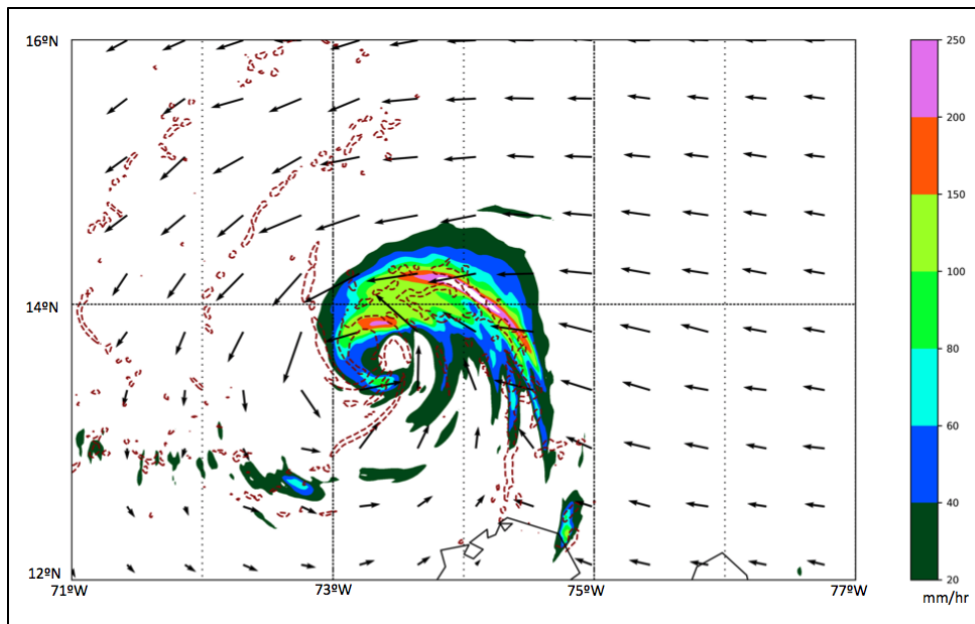


Figure 4.5: 10-m wind vectors (m/s), 3-hr accumulated precipitation (shaded, mm/hr) and divergence (dashed contours) less than $-1 \times 10^{-3} \text{ s}^{-1}$ in the CTL simulation valid at 0300 UTC 1 October 2016

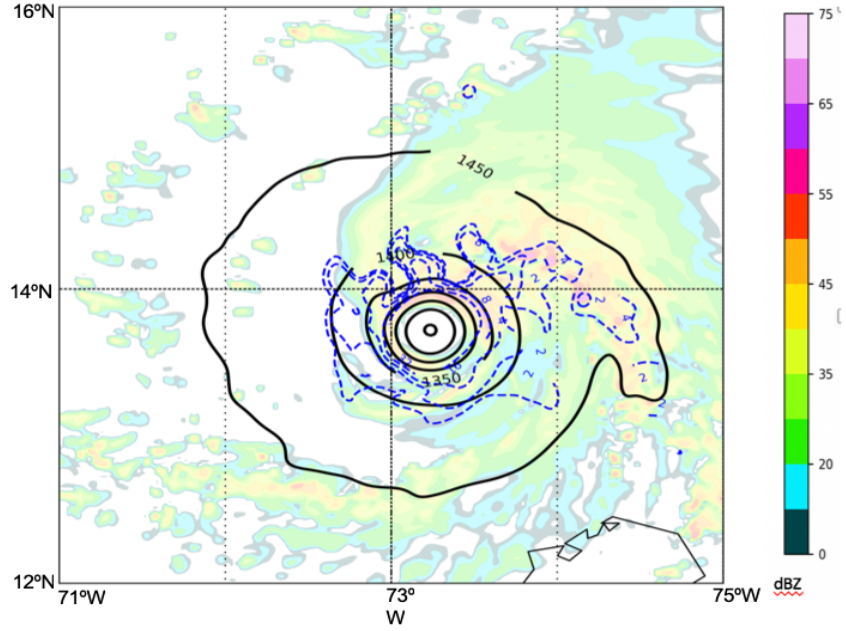


Figure 4.6: 850mb heights (solid contours, m), inertial stability greater than 2×10^{-7} (dashed contours, s^{-2}) and simulated reflectivity (shaded, dBZ) in the CTL simulation valid at 03 UTC 1 October.

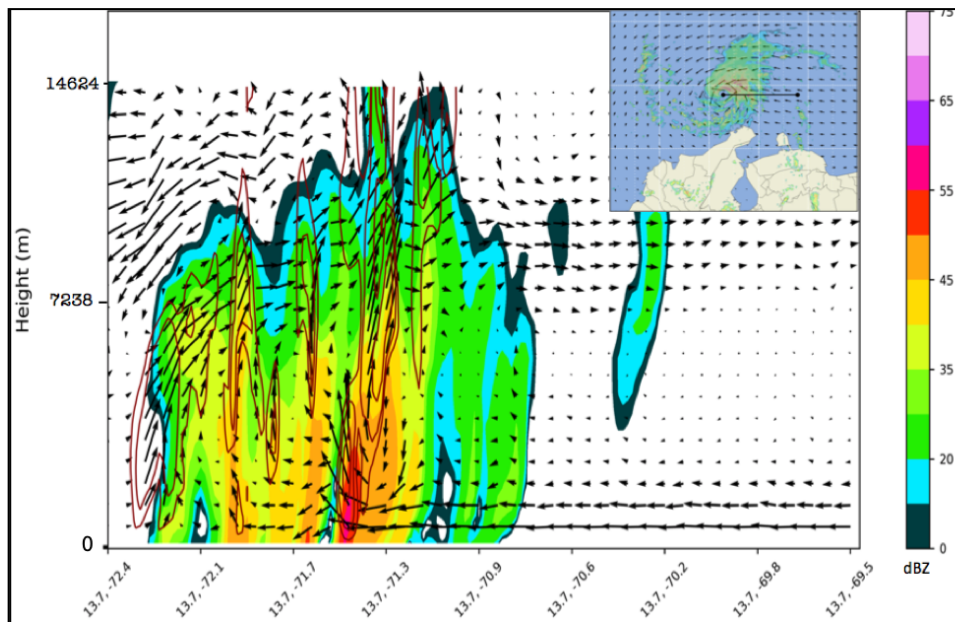


Figure 4.7: Cross section of Hurricane Matthew's reflectivity (dBZ), omega less than -1 m s^{-1} , and horizontal wind vectors in the CTL simulation valid at 0000 UTC 1 October.

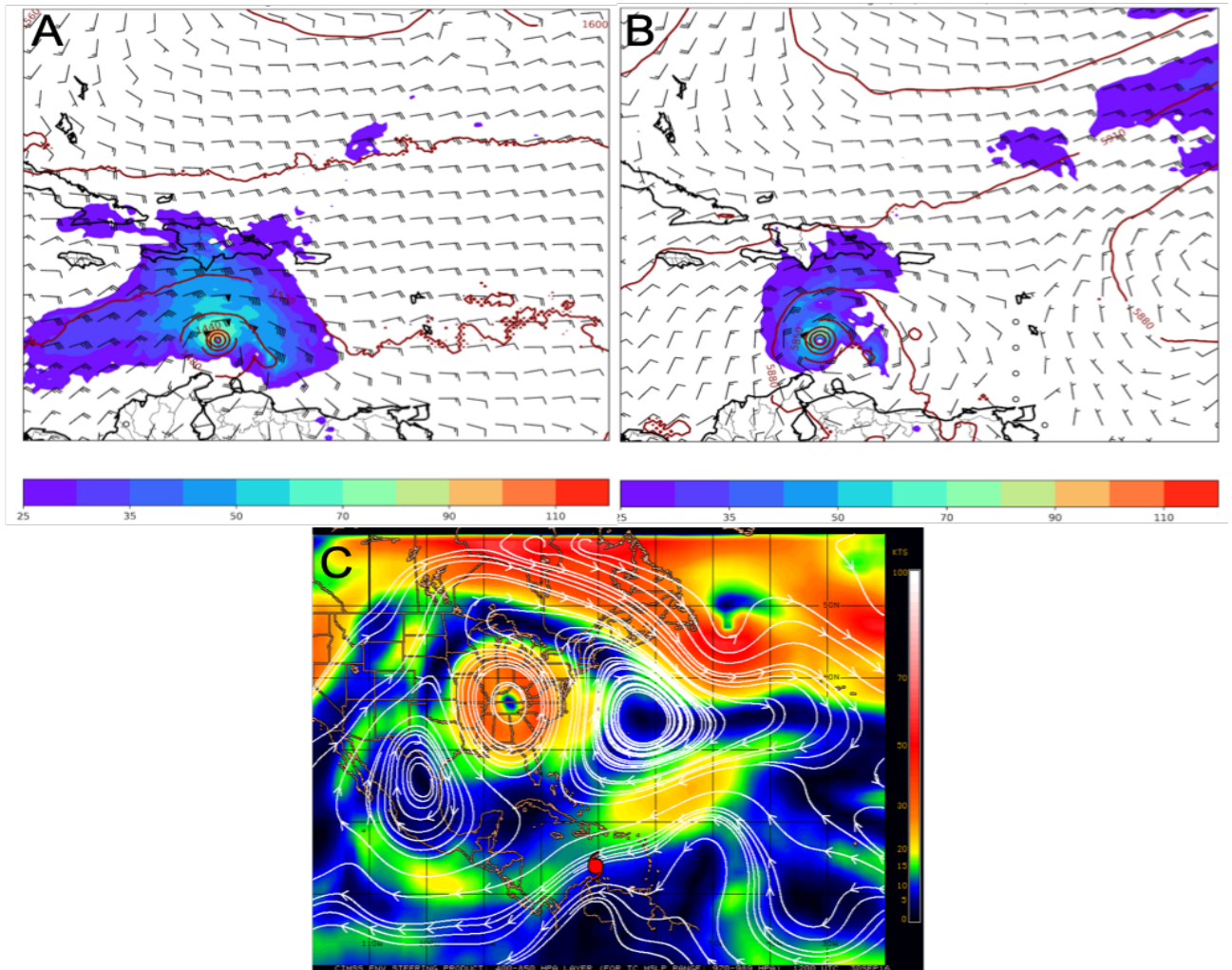


Figure 4.8: Geopotential heights and winds (vectors, kts) at (a) 850 mb and (b) 500 mb with winds >20 kts in solid contours and (c) 400 - 850mb deep layer mean steering flow from CIMMS TC archive (<http://tropic.ssec.wisc.edu/archive>). All images are valid at 12 UTC 30 September 2016.

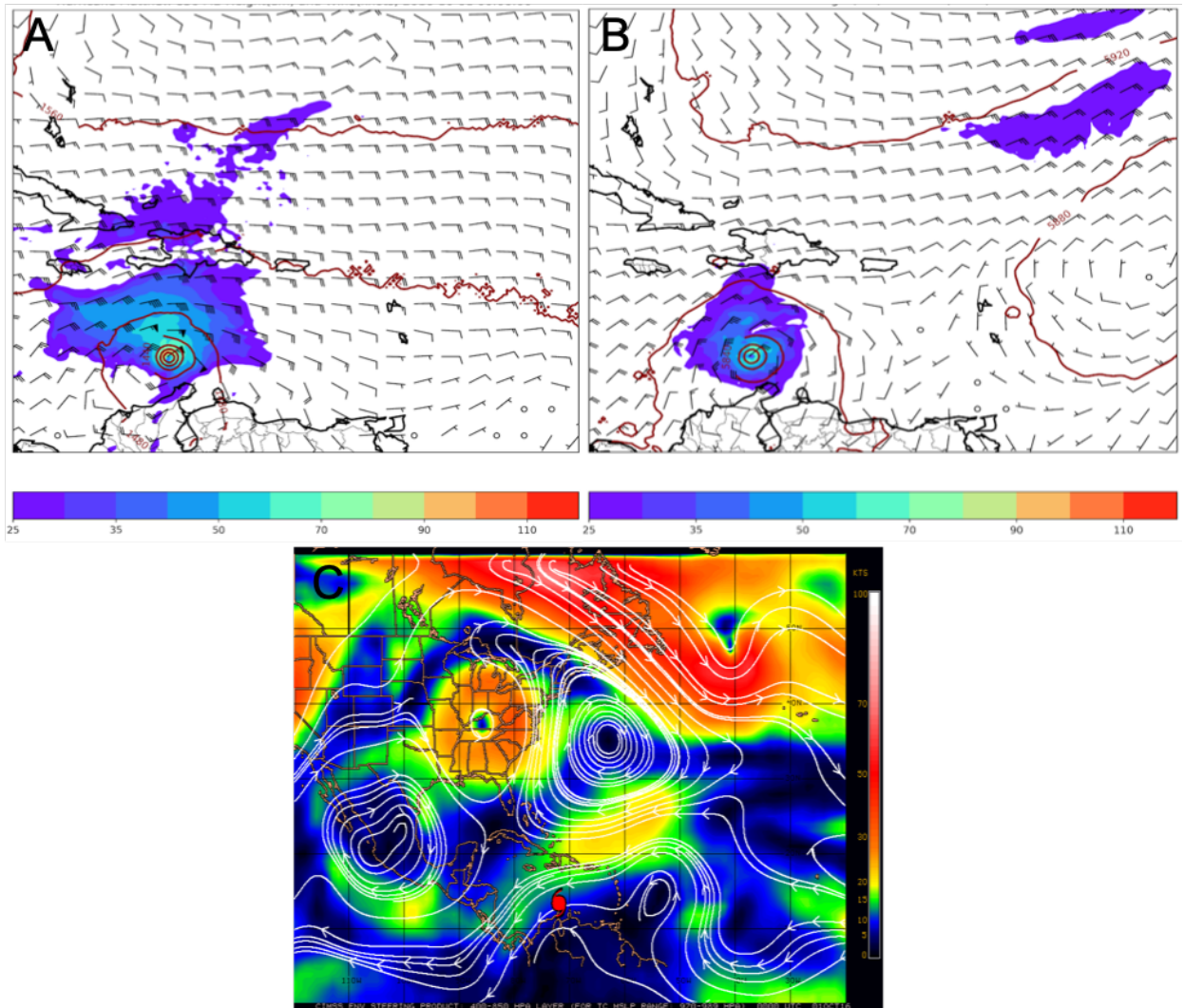


Figure 4.9: As in Fig. 4.8 but valid at 00 UTC 1 October 2016.

Chapter 5

REDUCED TERRAIN SIMULATION RESULTS

In this chapter, I discuss the results of the experimental reduced terrain simulation (T50) in comparison to the CTL simulation. Through these comparisons, I address the last two research questions proposed in Chapter 1, which focus on understanding the relationship between remote terrain on Hurricane Matthew's PRB and the relationship between remote terrain and TC inner core structure. In section 5.1, I concentrate on the similarities and differences in TC track and intensity in the CTL and T50 simulations to gain an overview on the T50 simulation. In order to gain a better grasp of the differences in inner core structure, I also analyze azimuthally averaged wind and temperature plots in this section. Section 5.2 specifically focuses on the differences in precipitation amounts and rainband structure between the CTL and T50 simulations. A more in-depth analysis of environmental conditions and stability near the persistent convection is discussed in section 5.3. Also in section 5.3, I address the thermodynamic environmental differences in relation to the modified terrain over northern South America.

5.1: Synoptic and Inner Core Structure Overview

Similar to section 4.1, I use best track and intensity time series to compare the T50 simulation to the CTL simulation. TC center is determined in the same way, by identifying the location of $MSLP_{\min}$ within the 2km domain (Fig. 4.1). The T50 simulation is initialized at 00 UTC 30 September in the same location as the CTL, approximately 0.25° northwest of the observed position. The T50 simulated TC track nearly mirrors that of the CTL for the first 30 hours after initialization, although with a slightly smoother (less north/south oscillation in) track. This similar track shows that the

T50 simulation also followed a path approximately 0.25° north of the observed TC during this time. After 30 hours post-initialization, the CTL simulation continues straight west while the T50 simulation follows a more parabolic curve to the northwest. The CTL simulation tracks back north following this timestep; however, the longer path caused a difference in translation speed allowing the T50 simulation to be slightly farther north from 36 hours post initialization until the end of the model run.

As in section 4.1, I use MSW at 10 meters and $MSLP_{\min}$ time series to compare the intensity of the T50 simulated TC with the CTL and observations (Fig. 4.2 & 4.3). The intensity trends from the CTL simulation were also seen in the T50 simulation with very similar strengthening and weakening phases from initialization to 03 UTC 01 October and 06 UTC 01 October to 18 UTC 01 October, respectively. Both model runs were unable to pick up on the RI observed in Hurricane Matthew. This result was expected as no prior research has suggested a relationship between terrain height and the onset of RI.

To analyze the differences in TC structure in the CTL and T50 simulations, I use azimuthally averaged cross sections of tangential and radial winds as well as warm core temperature anomalies. To create these plots, the average of the variable of concern is taken over a congruent radial bin to represent the axisymmetric TC structure. These averages were measured every 10 kilometers out to radius of 250 kilometers. Additionally, I perform time averages to smooth out high frequency variability at individual time steps. At 24 hours after initialization, the tangential wind (tangential component of wind with respect to the TC center) plots indicate a stronger radius of maximum winds (RMW) in the CTL simulation. This can be identified between 00 and 03 UTC 01 October (Fig 5.1). Observing the radial wind (normal component of the wind

with respect to the TC center) plots during this same time period, the outflow near the eyewall and RMW, below 3 kilometers, is much stronger in the T50 simulation (Fig 5.3). The stronger radial component in the eyewall could help explain why the RMW is weaker in the T50 simulation even though the maximum winds at 10 meters are similar. Time-averaged radial winds show another feature evident in the CTL simulation: stronger inflow near the surface of the CTL simulation near $r = 40$ kilometers. This stronger inflow measured in the CTL simulation may be due to a stronger warm core (see Fig 5.4 and discussion below). In the next 3 hours, between 03 and 06 UTC 01 October, the RMW becomes narrower in both simulations, but remains stronger in the CTL simulation (Fig. 5.2). Temperature anomalies are also plotted to show the strength and location of the warm core (Fig 5.4 & 5.5). For both 3-hour intervals, the CTL simulation has a stronger maximum temperature anomaly, which generally signals a stronger TC. As noted in section 4.1, the TC intensity in both simulations is similar, but it is important to note that TC intensity is measured with a single value ($MSLP_{min}$, 10-meter MSW) at one gridpoint while the warm core anomaly represents a more comprehensive picture of TC three-dimensional structure. Overall, the CTL simulation has stronger winds within the RMW and stronger inflow, consistent with a stronger warm core. The T50 simulation exhibits a weaker warm core and stronger near-surface and low-level outflow on the interior of the RMW, which is associated with a weakening and/or expanding low-level vortex.

5.2: Comparison of Reduced Terrain and Control Simulation Precipitation

An important step in identifying the impact of remote terrain on TC structure and rainband activity is to examine the precipitation itself. To accomplish this, model-

simulated reflectivity at 3500 meters above sea level and 3-hr accumulated precipitation (mm/hr) are plotted. Time steps prior to this (21 hours after initialization) are not used in this analysis due to underdevelopment of the primary and secondary rainbands (Fig. 5.9).

As stated in section 4.3, the CTL simulation produced a persistent convective feature to the northeast of the TC center with characteristics that are consistent with a PRB. This feature can be identified by examining reflectivity in the CTL simulation starting at 00 UTC 01 October (Fig. 5.6a). At the same time in the T50 simulation (Fig. 5.6b), this same convective feature appears farther from the TC center and is disconnected from the eyewall precipitation. Despite this difference in the location of the rainband, rainfall rates and reflectivity do not exhibit a large disparity. At 03 UTC 01 October, the rainband's connection to the eyewall in the T50 simulated TC becomes more distinguished but remains farther away from the TC center than in the CTL. This observation can be clearly recognized when analyzing the 3-hr precipitation totals from 00 to 03 UTC 01 October (Fig. 5.10). Differences in the radial winds may aid in explaining rainband variability between the two simulations. A stronger radially outward flow near the eyewall, as seen in figure 6b, along with a weaker warm core represents an expanding and weakening TC. This difference in the T50 simulation could support the justification on why this convective feature is farther from the TC center. Other rainbands, which can be classified as secondary rainbands (Willoughby et al. 1984), south of the TC center also appear to be more developed at this time in CTL compared to T50 (Fig. 5.7).

Later, at 06 and 09 UTC, this same convective feature, however weaker, remains in the CTL simulation, whereas the rainband is smaller and farther away from the TC center in the T50 simulation (Fig. 5.8). Very little convection exists at 06 UTC 01

October in the southern portion of the T50 TC, where secondary inner core rainbands were present in the CTL TC (Fig. 5.8). Analyzing the 3-hour precipitation totals over this time period (Fig. 5.11) yields similar interpretations while also highlighting an outer MCS that forms southeast of the TC center. Also of note, the TC eyewall is more degraded and less circular in the T50 simulation (Figs. 5.01-5.11), consistent with a weaker warm core (Figs. 5.4-5.5), although both TCs are weakening with time. After 09 UTC 01 October, as noted in the intensity time series, both simulated TCs undergo significant weakening, which prevents further analysis of inner core rainbands at these later time steps.

5.3: Comparison of Reduced Terrain and Control Simulation Thermodynamics

Between 03 and 09 UTC 01 October, both simulations initiate continuous convection to the southeast of the TC center. This convection could be a factor in prolonging the longevity of the rainband east of the TC center where the PRB was identified in section 4.3. Also, the continuous convection is developing downstream of terrain with elevations between 500 and 1000 meters, and elevations greater than 2000 meters further upstream. An atmospheric layer downstream of terrain has been noted to alter the thermodynamics of that layer. In this section, I analyze skewed temperature with logarithmic pressure (skew-T) plots and equivalent potential temperature cross sections. These graphics are utilized to assess the thermodynamic environment in the area of convection initiation downstream of the terrain.

Single model gridpoint skew-T plots are likely to display large variability due to influences from small scale processes. To minimize those effects, temperature and dewpoint temperature are averaged over a box between 12.8°N and 13.2°N latitude, and

72°W and 71°W longitude, a region that displayed continuous convective initiation enveloped in the TC circulation. At 00 UTC 01 October, the skew-T plots for the CTL and T50 simulations (Fig. 5.12) show similar temperature and dewpoint temperature lapse rates with the only exception being a slightly drier mid- to upper-levels in the T50 simulation. The pattern changes when analyzing the skew-T at 03 UTC 01 October (Fig. 5.13). A larger contrast in dewpoint temperature can be identified, with a drier surface in the CTL simulation. Downslope flow off of the terrain may be causing air parcels to adiabatically warm, which could be leading to a drier near-surface layer in the CTL simulation. Also of note at this time step, the CTL skew-T is near saturation between 600 and 500 millibars. In contrast, the T50 skew-T indicates a larger temperature and dewpoint temperature difference in this layer, suggesting more convection present within the averaged box in the CTL simulation. The skew-Ts at 06 UTC 01 October depict a similar profile to that presented in Figure 15.

Because the skew-T in Figures 14-15 are difficult to compare visually, I have created tables of temperature (Table 1) and dewpoint temperature (Table 2) differences (CTL minus T50) for altitudes from 250 to 2000 meters, every 250 meters. Below 2000 meters represents a near boundary layer section of the atmospheric profile, where the greatest temperature and dewpoint temperature differences occur. For all four timesteps, the CTL simulation tends to have a drier boundary layer (Table 2), which is in agreement with the skew-T profiles. Temperature is also slightly different between the CTL and T50 simulation. Except for at 03 UTC 01 October, the boundary layer temperature in the CTL simulations is slightly colder than the T50 simulation. This difference strengthens with time and vertical level, reaching maximum values of around 0.2 degrees Celsius at 09 UTC 01 October.

For the dewpoint temperature and temperature datasets, I use a one-sided pooled t-test to determine whether statistically significant differences exist between the T50 and CTL simulations. The t-test is a statistical tool used to evaluate differences in the means of two groups. I use a pooled t-test because the variances in the CTL and T50 data are similar. Testing the statistical significance in the contrast of temperature gives a probability value (p -value) of 0.0756. For a confidence threshold of 95%, this difference in temperature between the two simulations is not significant. However, the dewpoint temperature differences yield a p -value of less than 0.0001, identifying significantly drier lower levels in the CTL simulation. This result is consistent with a hypothesis that downslope motion off the terrain of South America could be leading to a drier air mass on the lee side of the mountains, potentially contributing to increased instability in the CTL versus T50 simulation. Under this hypothesis we would also expect warmer boundary layer conditions due to adiabatic warming. The results with respect to temperature suggest some cooling but are inconclusive.

Alterations to temperature and dewpoint temperature downstream of the terrain should impact the moist static stability of the layer, when comparing the CTL and T50 simulations. Moist static instability can be observed when equivalent potential temperature decreases with height. To analyze the moist static stability within the region of convective initiation, vertical profiles of equivalent potential temperature (θ_e) are evaluated. At 00 UTC 01 October (Fig. 14), the equivalent potential temperature cross section depicts a similar profile to the cross sections in Li and Wang (2012) with smaller lapse rates in the inner core (west of 72°W) than the outer core. This atmospheric profile is in agreement with the understanding of TC rainband convection. Inner core convection is initiated through dynamical processes such as convergence. Because of this, less

instability and even moist neutral (Emanuel 1986) conditions are commonly observed in the TC eyewall. In the outer core, convection is also dynamically driven, but larger localized instability is required for convection, especially in distant rainbands. As the TC moves west with time, the outer core envelops most of the cross section (Fig. 5.15), showing that the newly developed convection after 03 UTC 01 October is initiating within the outer core (Fig. 5.7). To quantify this, average equivalent potential temperature lapse rates between 500 and 2500 meters were extracted at 72°W, 71.5°W, and 71°W (Table 3). Overall, lapse rates in the T50 simulation are larger than in the CTL simulation. This is contrary to the hypothesis that equivalent potential temperature lapse rates downstream of higher terrain should be larger. Even though this conflicts with expectations, the lapse rate difference did not show statistical significance based on an unpooled (unequal variance) t-test ($p = 0.0951$).

5.4 Summary of Terrain Impacts on the PRB and TC Structure

At a first glance, the T50 and CTL simulation appear mostly similar in structure and intensity. Both TC tracks and intensities follow similar paths and trends, respectively, when analyzing the time series plots. Upon further analysis, variations between the two simulations surfaced. Azimuthally averaged cross sections of tangential and radial winds depict a more quickly weakening TC in the T50 simulation in comparison to the CTL simulation between 00 and 06 UTC 01 October. This is in accord with the azimuthally averaged temperature anomaly plots, which show a weaker warm core in the T50 simulation. Comparison of the CTL and T50 precipitation reveals a PRB that is similar in peak intensity but different in geographic location. In comparison with the CTL, the T50 PRB is farther away from the TC center. At later timesteps, the T50 PRB dissipates while the CTL PRB, although weaker, persists for longer. Secondary rainbands to the south of

the TC center also indicate dissipation of convection in the T50 simulation over time. Continuous convective initiation downstream of terrain is proposed as one factor influencing the longevity of the PRB. Thermodynamic profiles of this region reveal a significantly drier boundary layer in the CTL simulation. Although not statistically significant, the thermodynamic profiles also show a warming trend in the T50 simulation, along with stronger negative equivalent potential temperature lapse rates. Overall, these results provide some evidence to support the hypothesis that remote terrain can influence TC convective structure by weakening the rate and coverage of convective initiation in the region downstream of the northern South America topography. Yet, some results are inconclusive or suggest some discrepancies with the hypothesized physical mechanisms (including modifications to vertical distribution of equivalent potential temperature). Future research (discussed in chapter 6) is needed to resolve these discrepancies.

Chapter 5 Figures

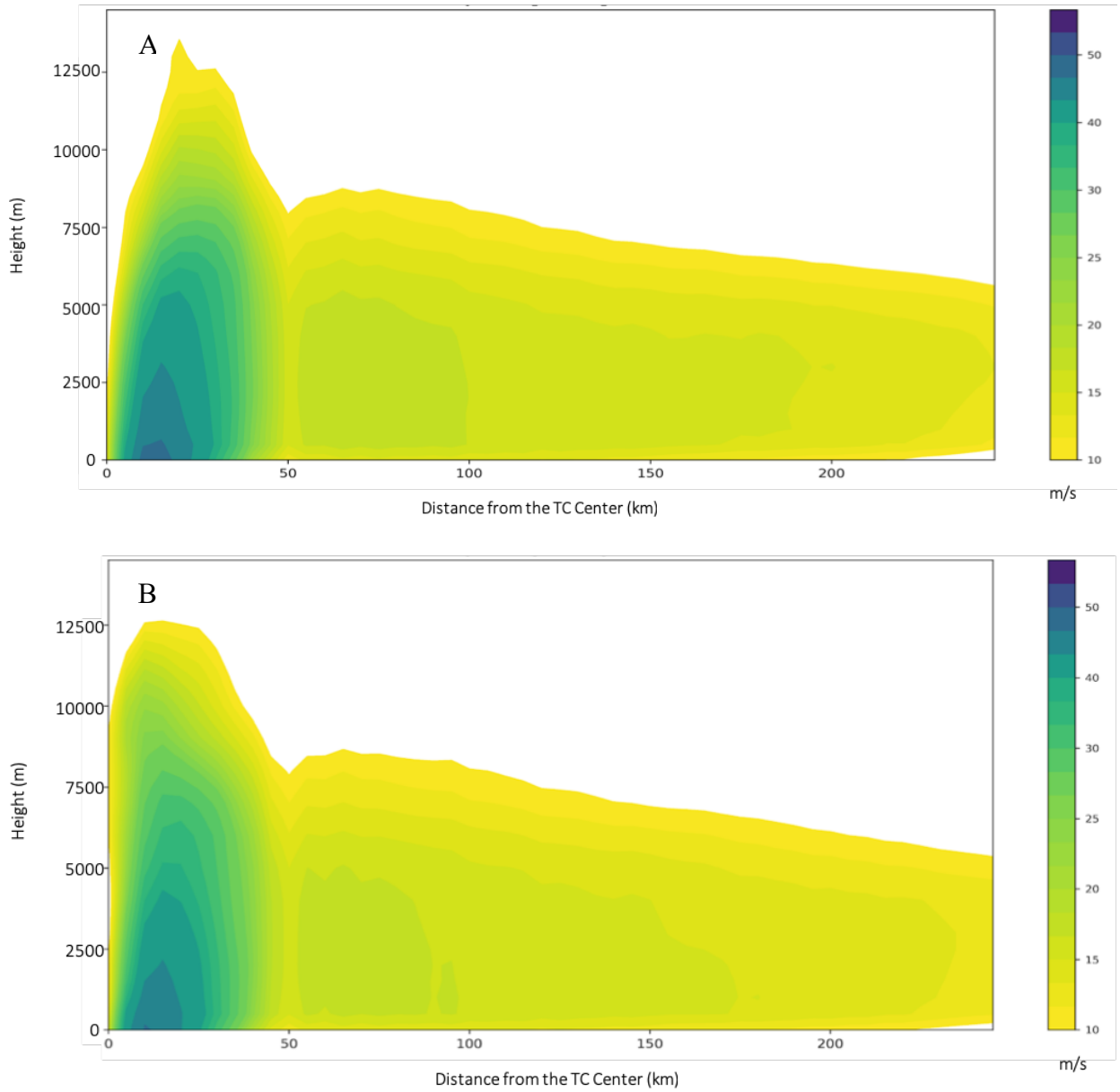


Figure 5.1: Vertical radial cross sections of azimuthally averaged tangential winds for CTL (A) and T50 (B) simulations, calculated horizontally at $r=5$ km intervals out to 250 km and vertically at 500 m intervals up to 15 km. Azimuthally averaged tangential winds are extracted every 30 min between 00 and 03 UTC 01 OCT and temporally averaged.

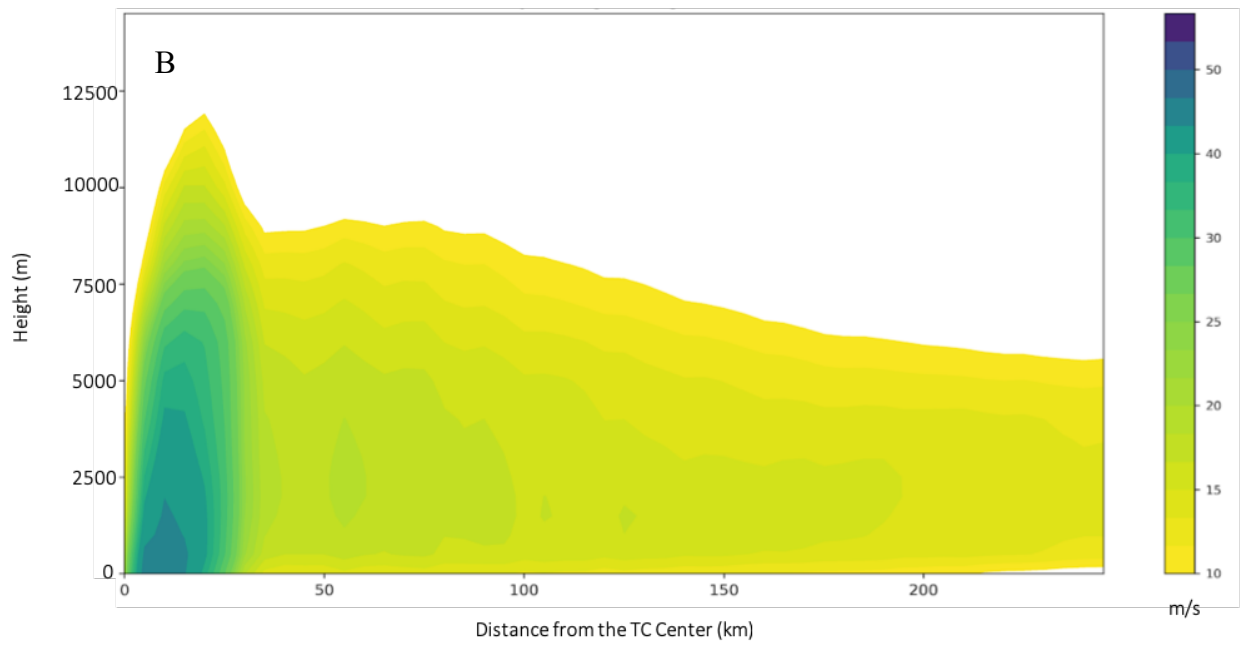
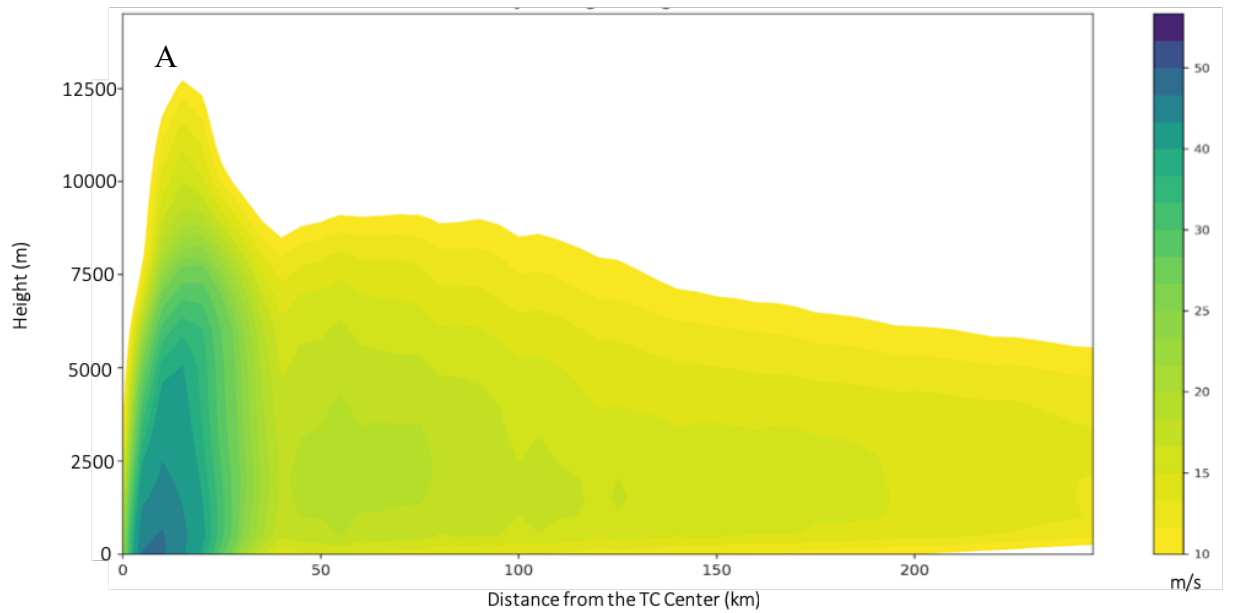


Figure 5.2: As in 5.1, but temporally averaged between 03 and 06 UTC 01 October.

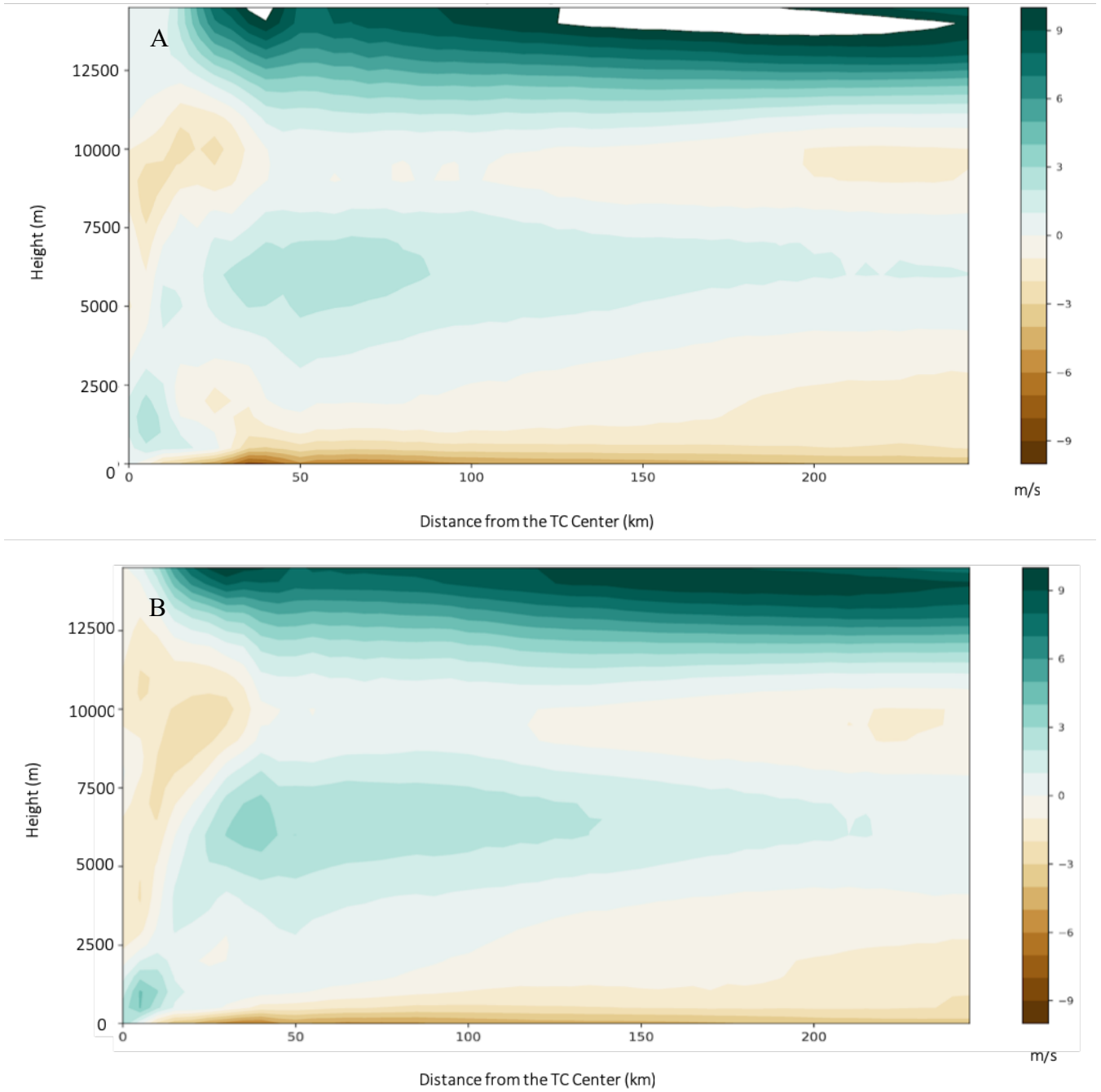


Figure 5.3: As in Fig 5.2, but with azimuthally averaged radial winds extracted every 30 min between 00 and 03 UTC 01 OCT and temporally averaged.

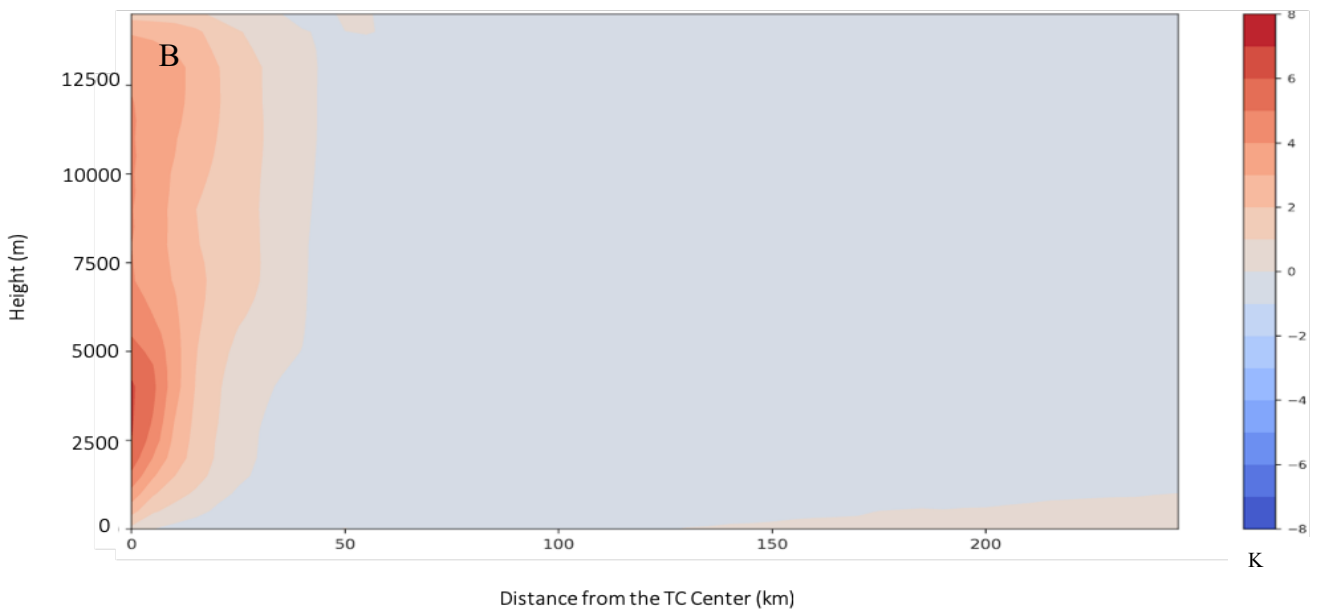
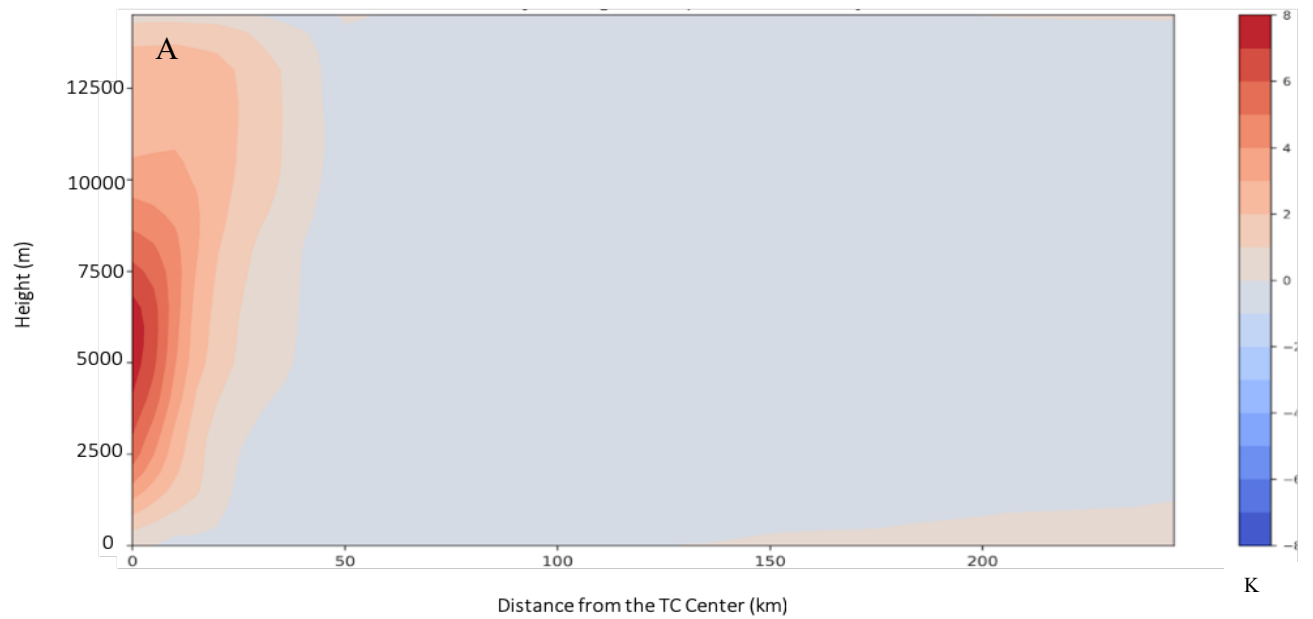


Figure 5.4: Vertical radial cross section of azimuthally averaged temperature difference from the average at each vertical level for CTL (A) and T50 (B) simulations, calculated every 5 kilometers out to 250 kilometers and every 500 meters up to 15 kilometers. Temperature differences are extracted between 00 and 03 UTC 01 OCT and temporally averaged.

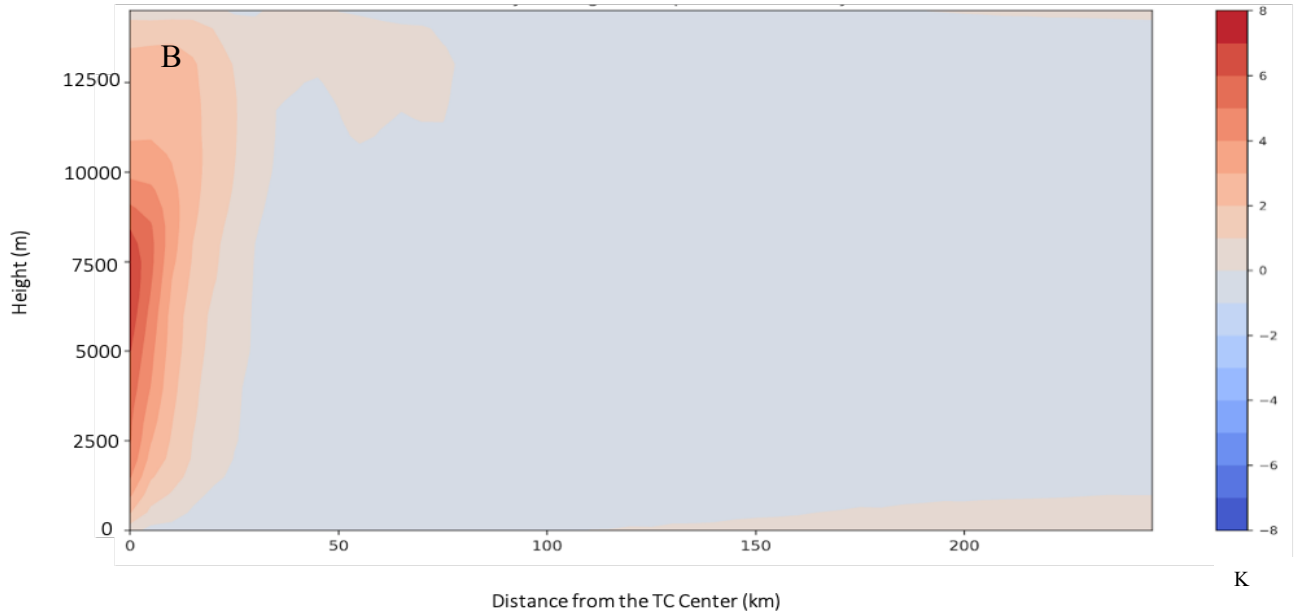
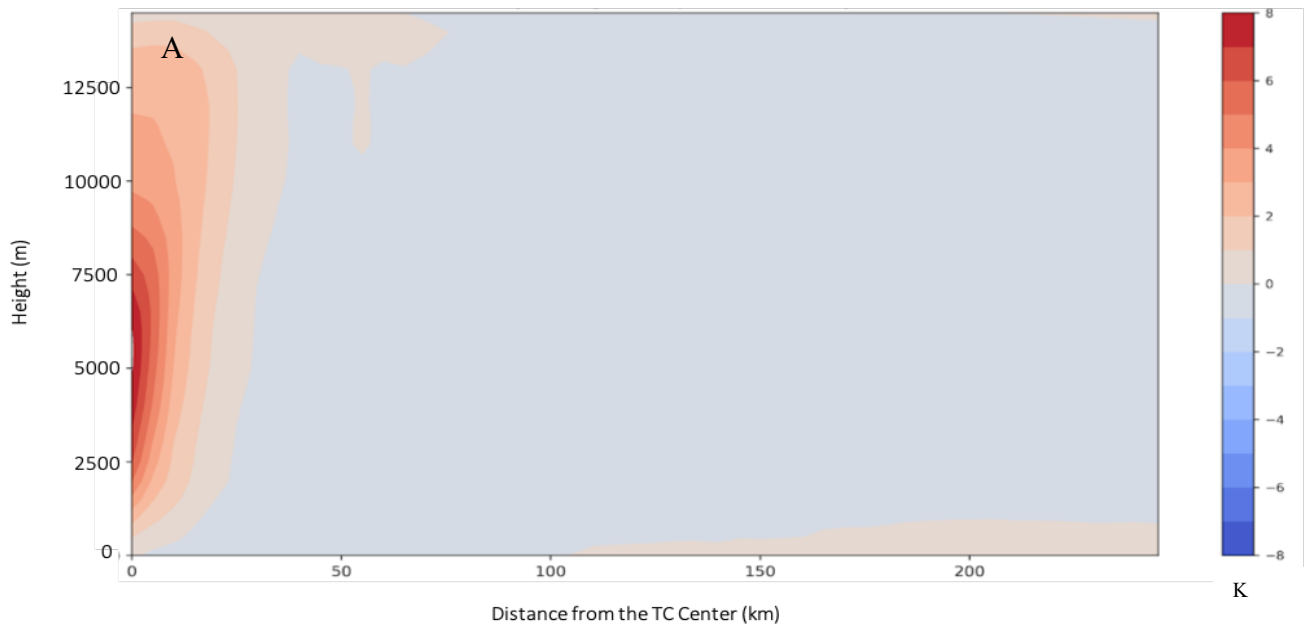


Figure 5.5: As in Fig. 5.4, but with a temporal average between 03 and 06 UTC 01 October.

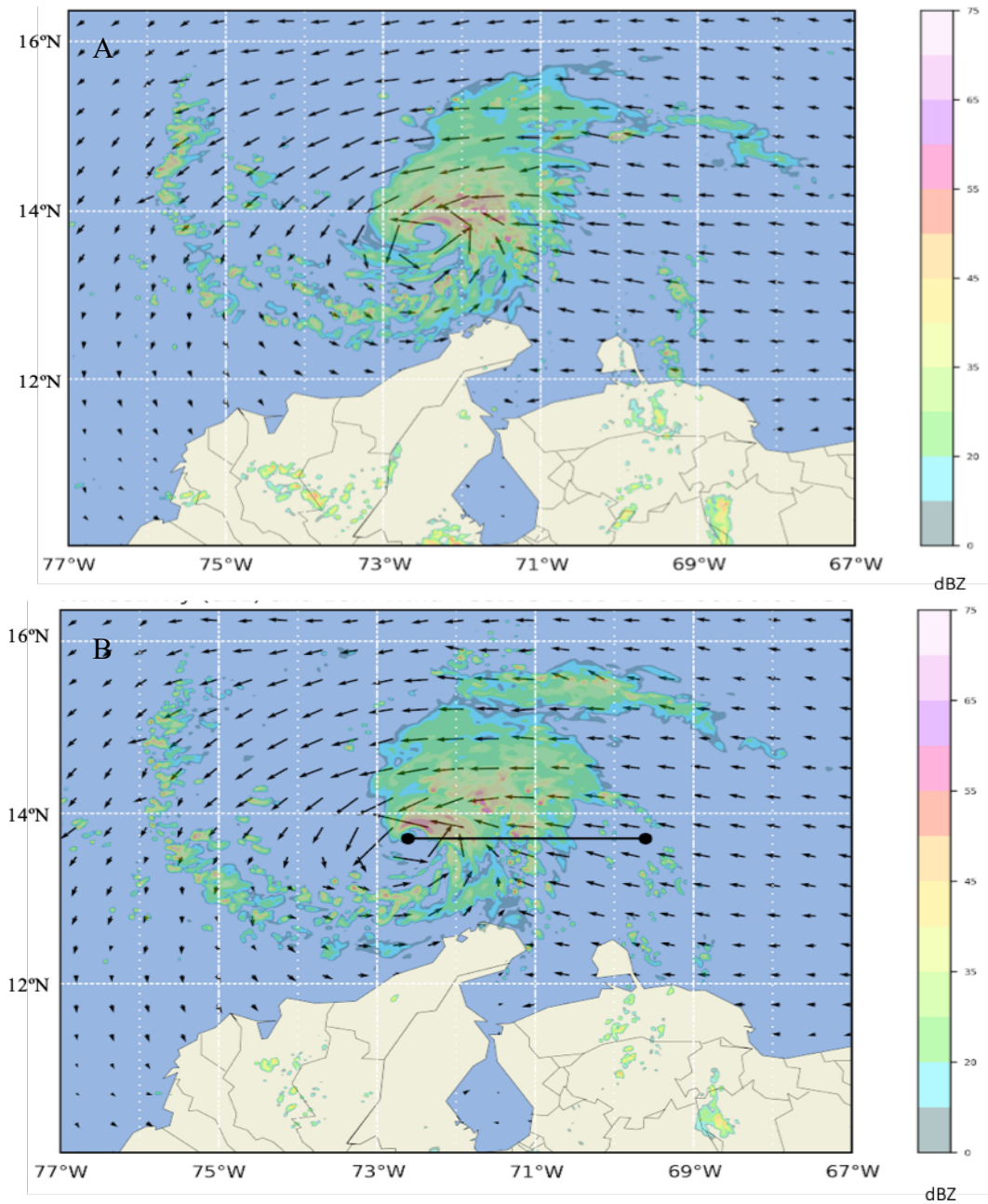


Figure 5.6: 10-m wind vectors (m/s), and 3500-m reflectivity (shaded, dBZ) in the CTL simulation (A) and T50 simulation (B), valid at 00 UTC 01 October.

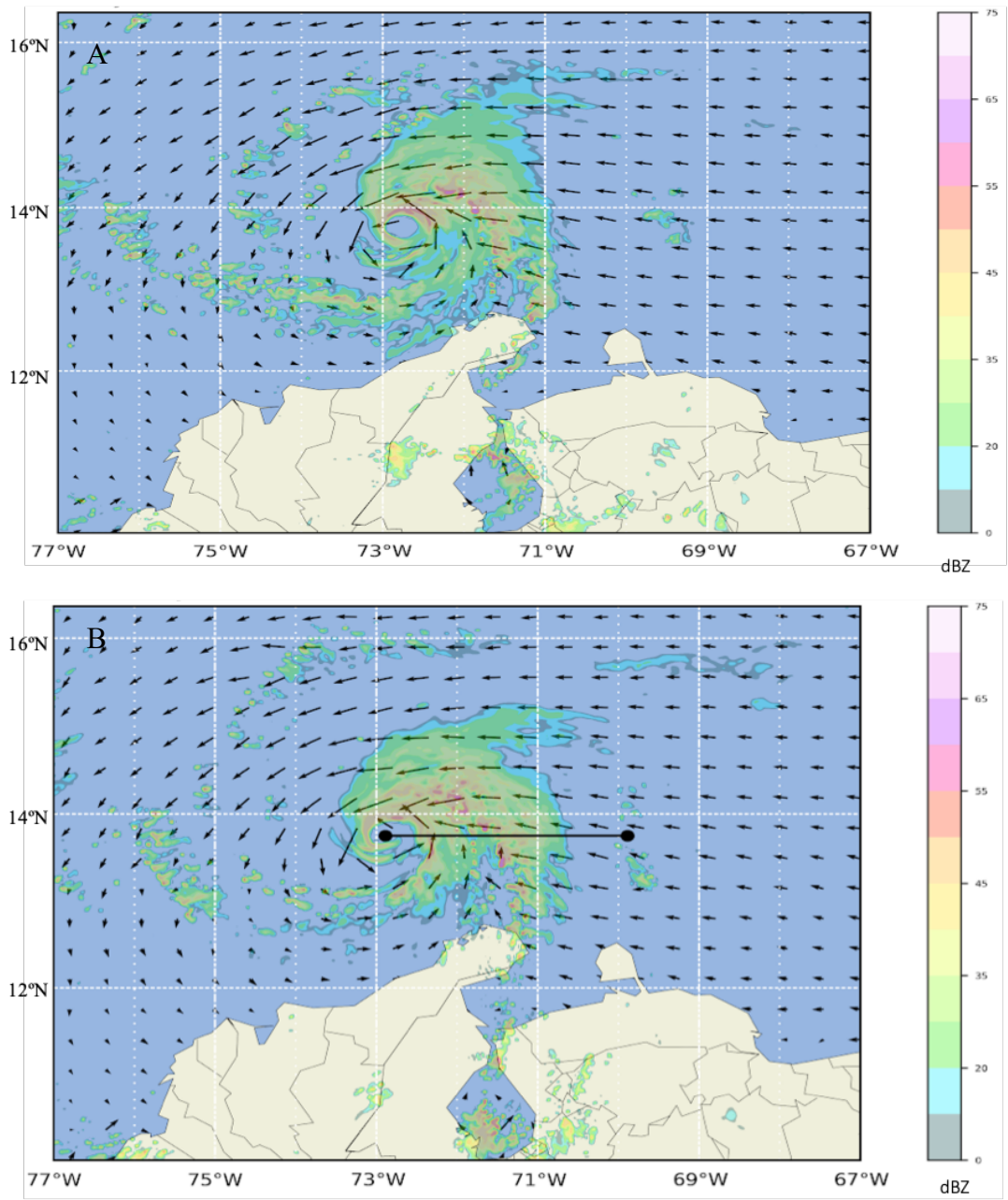


Figure 5.7: As in Fig. 5.6, but valid at 03 UTC 01 October

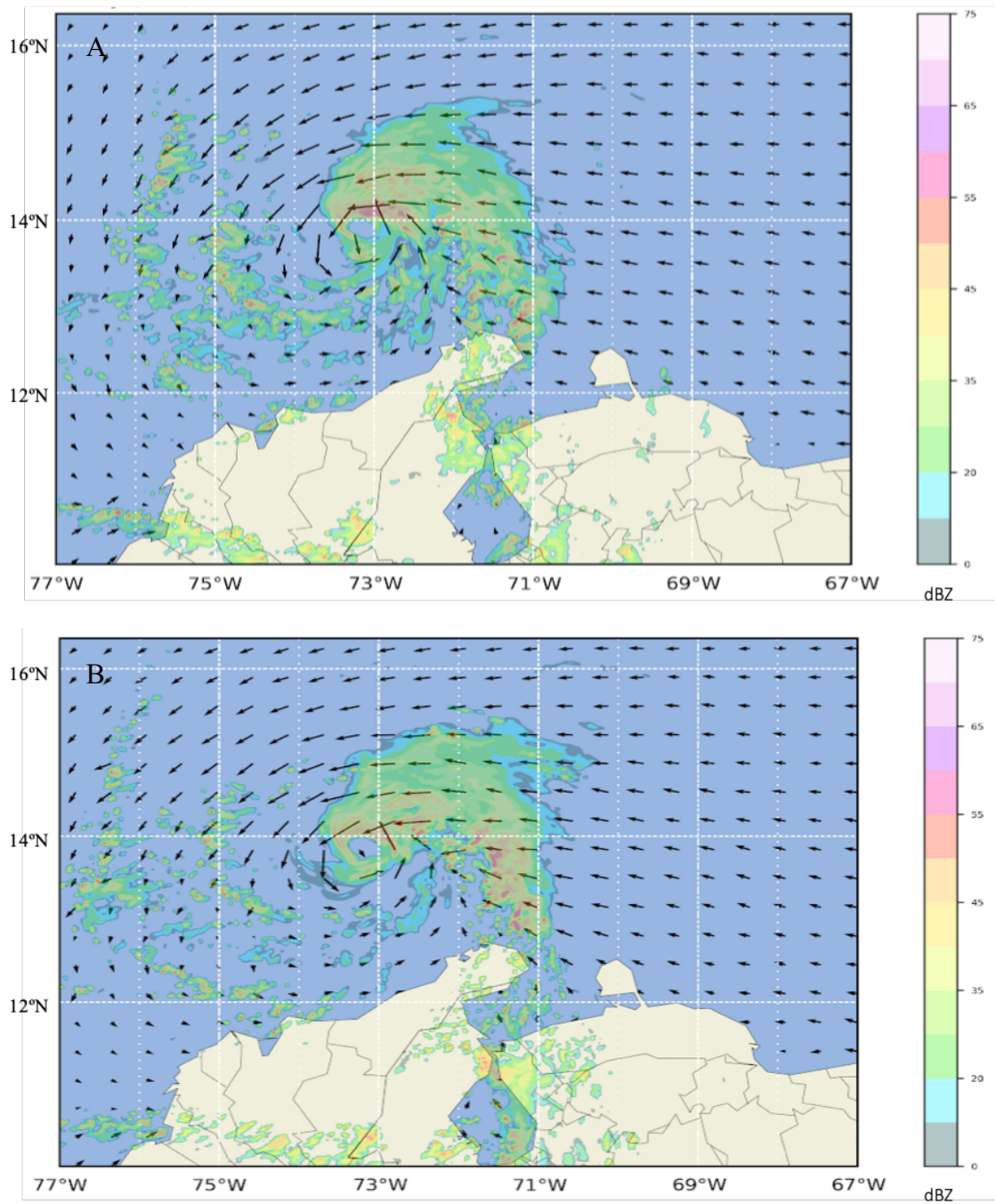


Figure 5.8: As in Fig. 5.6, but valid at 06 UTC 01 October

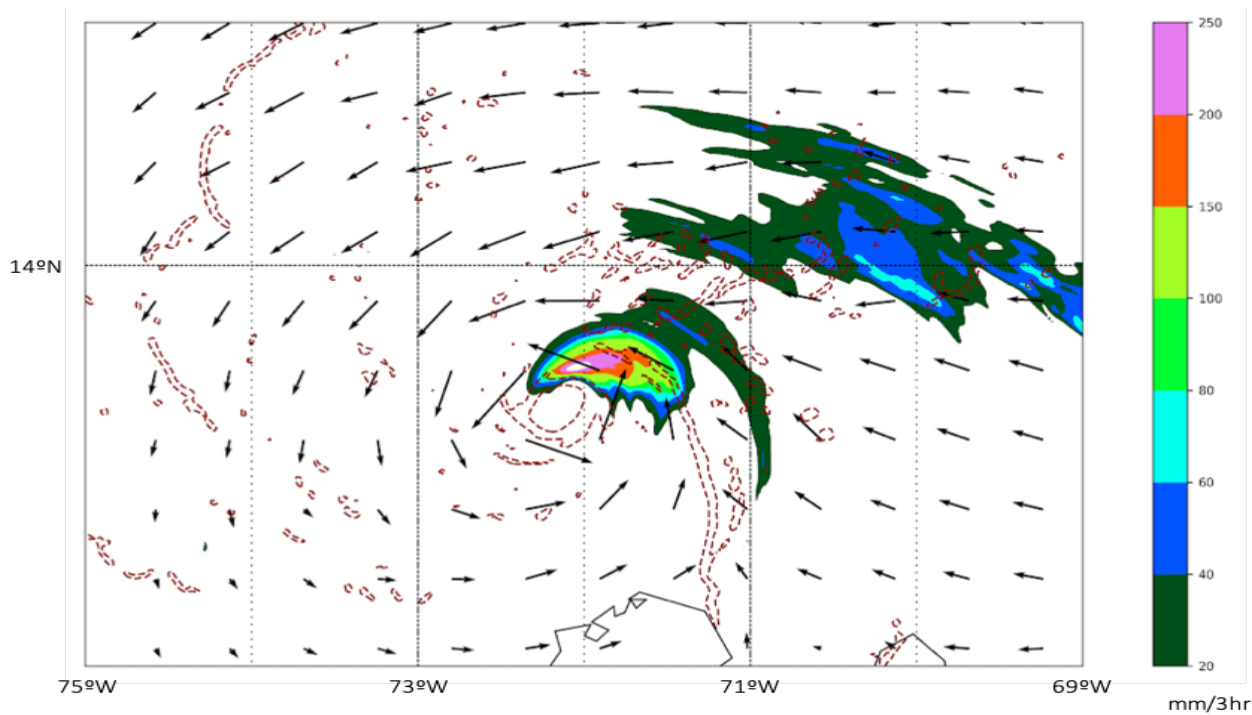


Figure 5.9: 10-m wind vectors (m/s), 3-hr accumulated precipitation (shaded, mm/hr) and divergence (dashed contours) less than $-1 \times 10^{-3} \text{ s}^{-1}$ in the CTL simulation valid at 21 UTC 30 September

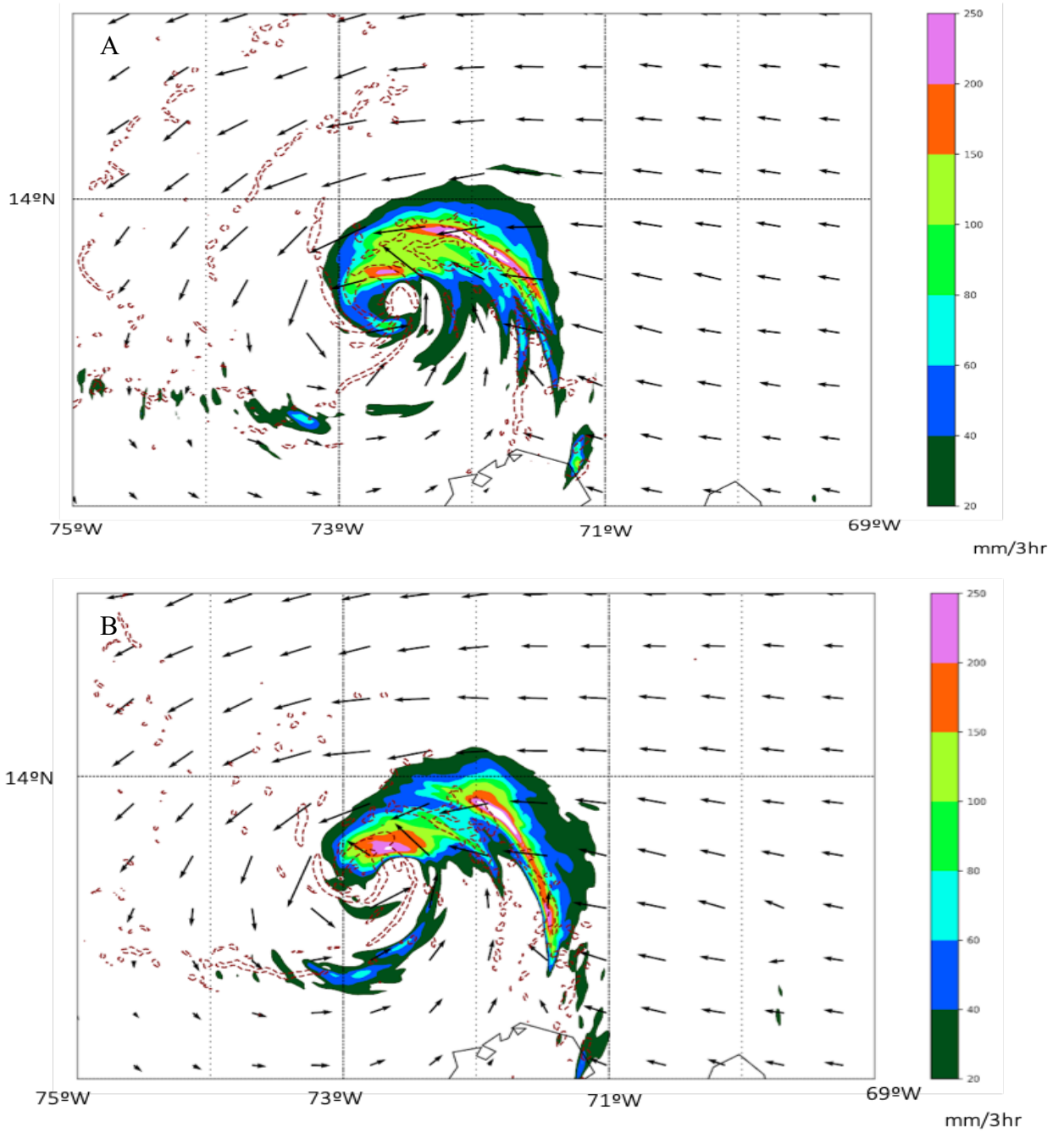


Figure 5.10: As in Fig. 5.9, but valid at 03 UTC 01 October, and with both CTL (A) and T50 (B) simulations.

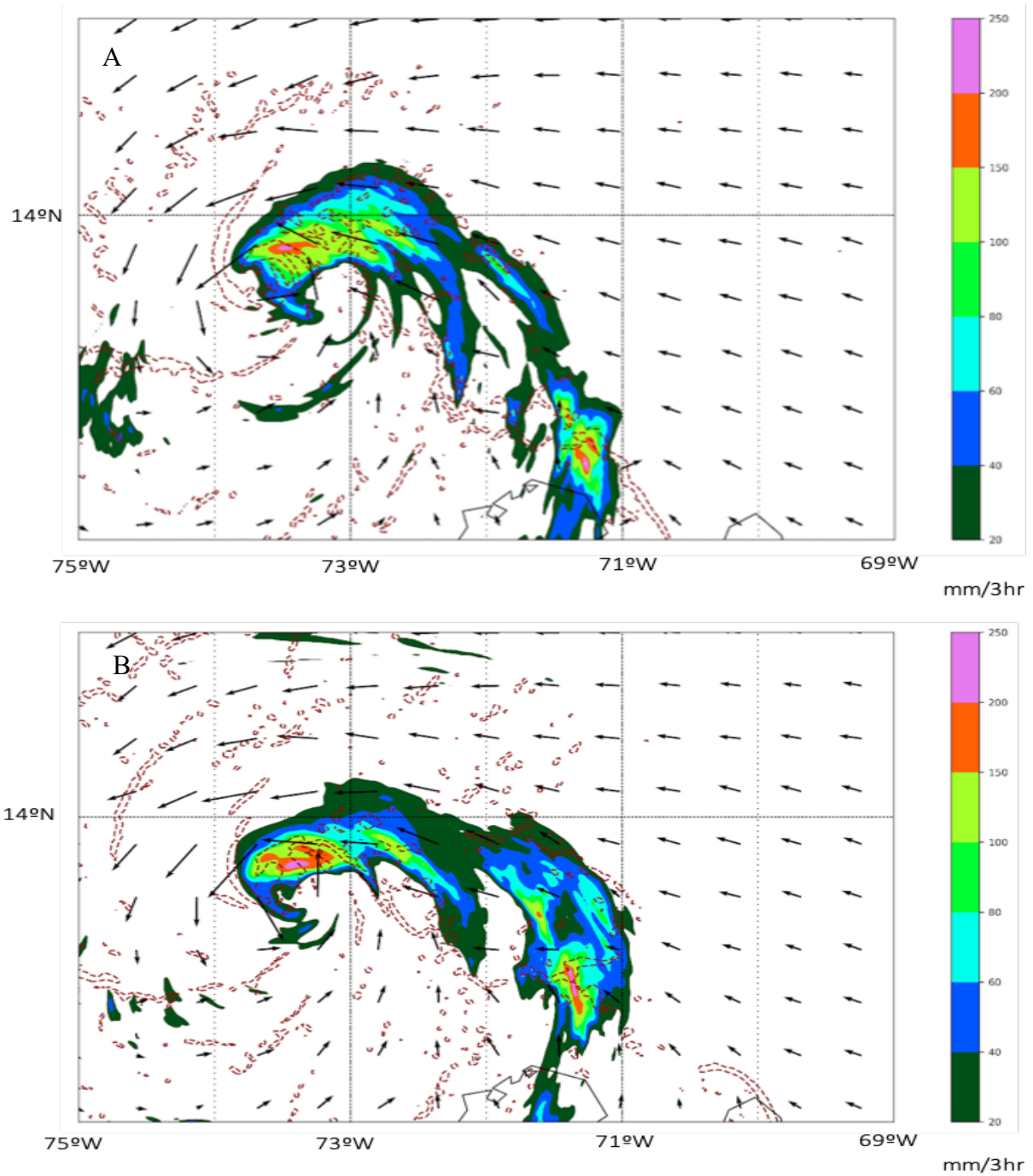


Figure 5.11: As in Fig. 5.10, but valid at 09 UTC 01 October

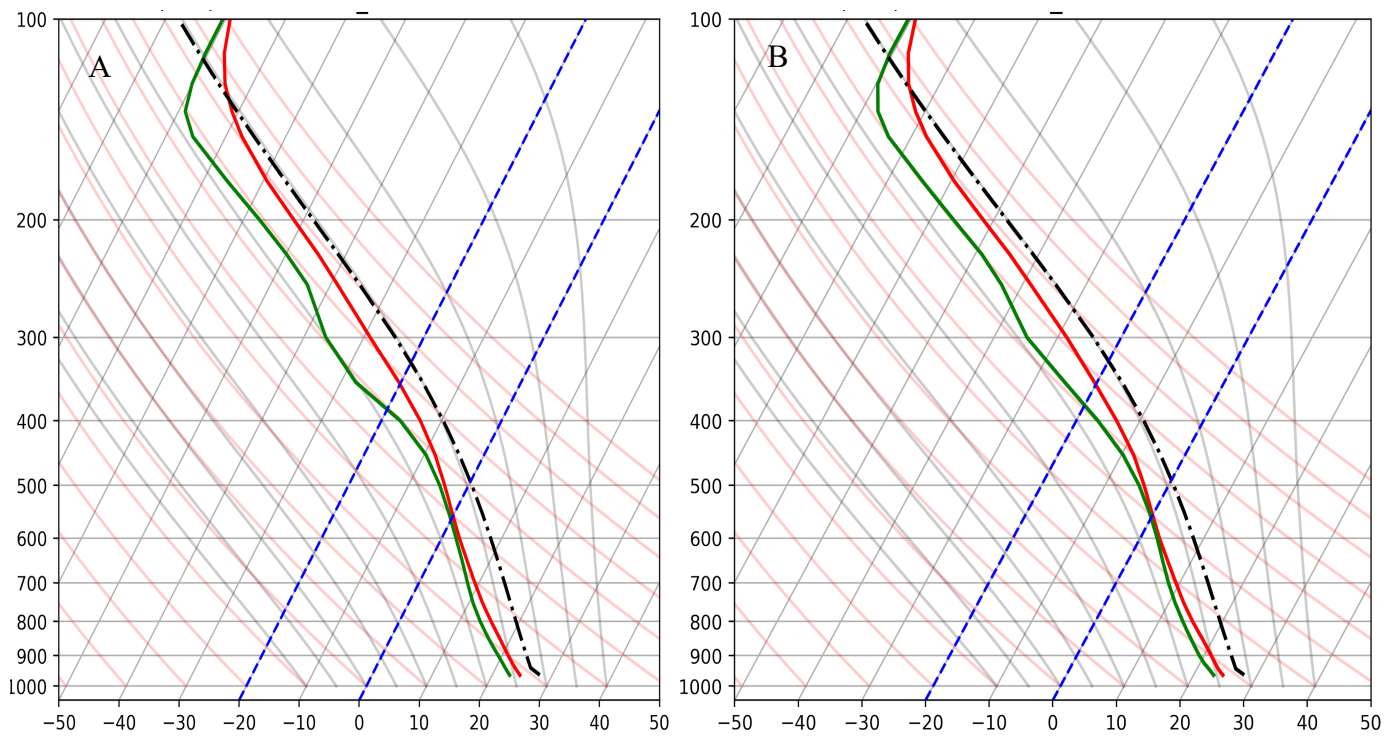


Figure 5.12: Temperature (red) and dewpoint temperature (green) plotted on skewed temperature (x-axis) and logarithmic pressure (y-axis) for the CTL (A) and T50 (B) simulations. Plots are valid at 00 UTC 01 October

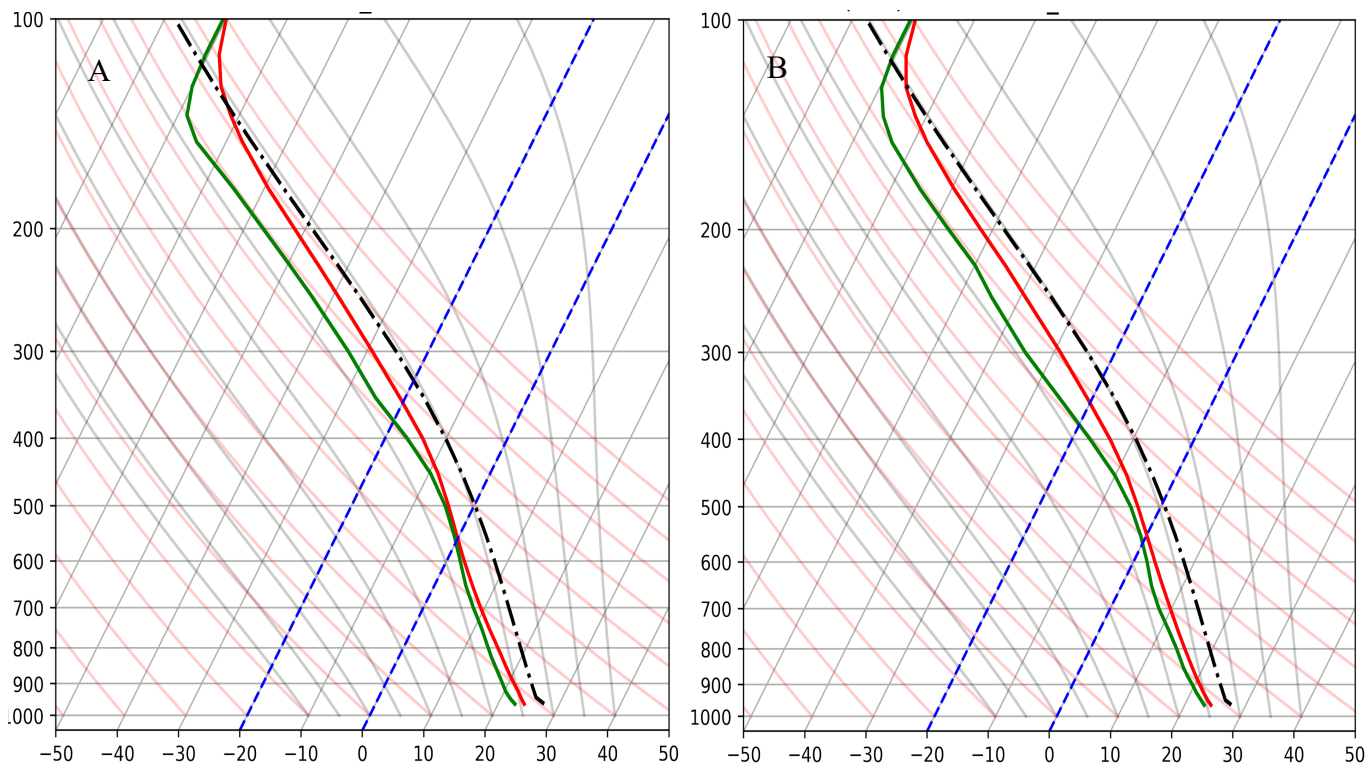


Figure 5.13: As in Fig. 5.12, but valid at 03 UTC 01 October.

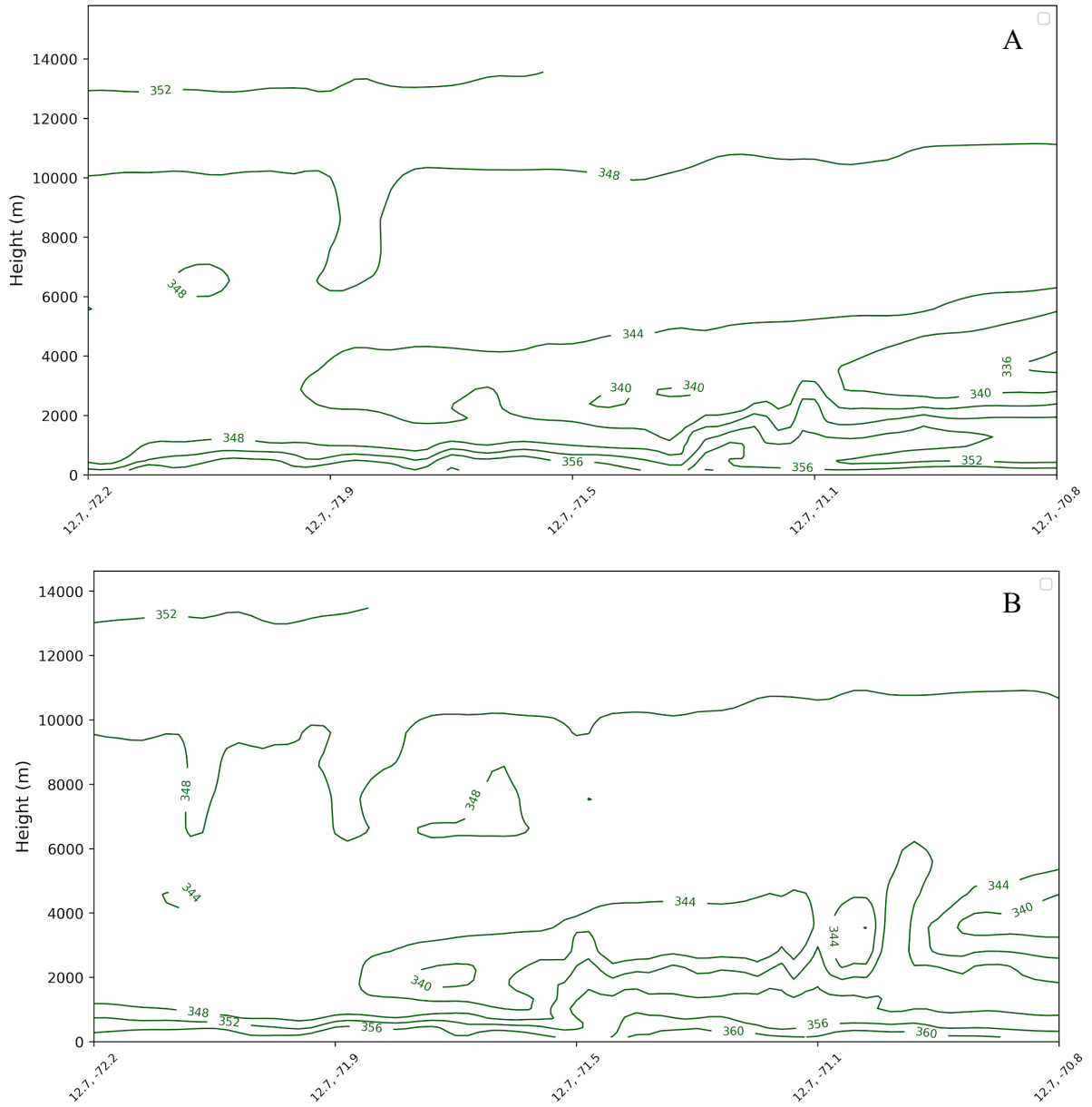


Figure 5.14: Vertical cross section of equivalent potential temperature (K) in the CTL (A) and T50 (B) simulations at 12.75°N along line segment between 72.25°W and 70.75°W showing thermodynamic structure in the inner core (west of 72°W) and through rainbands in the outer core (east of 72°W). Vertically, measurements are plotted between the surface and 14 kilometers. Graphic is valid at 00 UTC 01 October.

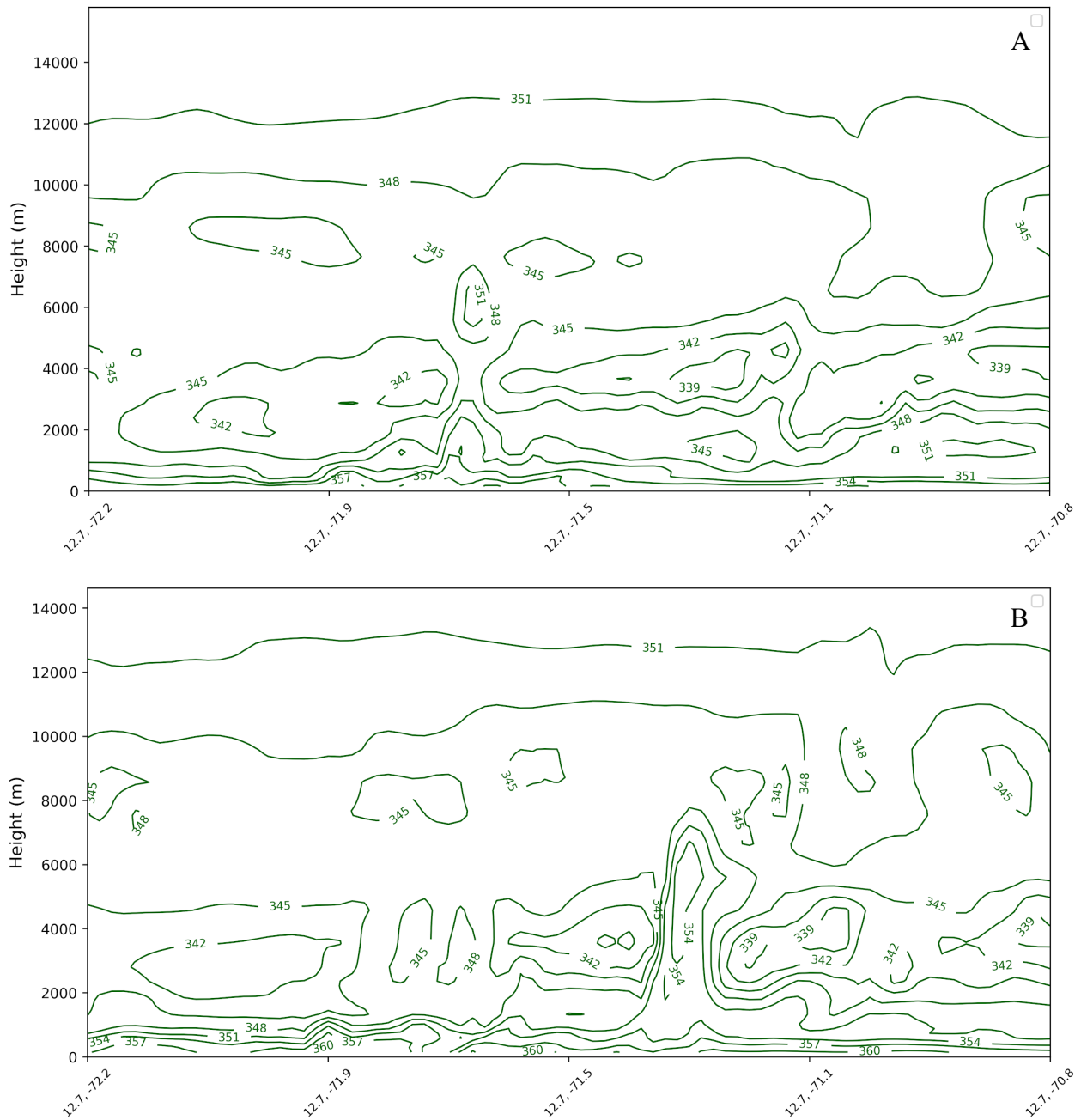


Figure 5.15: As in Fig. 5.14, but along line segment between 72.25°W and 70.75°W showing thermodynamic structure in the outer core valid at 03 UTC 01 October.

Chapter 5 Tables

Table 5.1: Differences in temperature (T) (°C) in the lower levels of the skew-T captured in Fig. 5.12 and 5.13. Differences are calculated by subtracting T50 values from CTL values.

Temperature Difference (°C)				
Height (m)	00 UTC 01 OCT	03 UTC 01 OCT	06 UTC 01 OCT	09 UTC 01 OCT
250	-0.02114	-0.02415	-0.34859	-0.16818
500	0.05115	0.10850	-0.16709	-0.17510
750	-0.03799	0.24080	-0.05949	-0.24572
1000	-0.13960	0.18015	-0.07578	-0.29120
1250	-0.12721	0.11549	-0.11977	-0.27756
1500	-0.09649	0.06883	-0.14077	-0.25807
1750	-0.05377	0.03381	-0.14669	-0.23596
2000	-0.03304	-0.03543	-0.12724	-0.23541

Table 5.2: Differences in dewpoint temperature (Td) (°C) in the lower levels of the skew-T captured in Fig. 5.12 and 5.13. Differences are calculated by subtracting T50 values from CTL values.

Dew Point Temperature Difference (°C)				
Height (m)	00 UTC 01 OCT	03 UTC 01 OCT	06 UTC 01 OCT	09 UTC 01 OCT
250	-0.21679	-0.28003	-0.3709	-0.0878
500	-0.20024	-0.60170	-0.6407	-0.1747
750	0.08454	-0.63130	-0.6176	-0.2941
1000	0.09542	-0.47272	-0.4177	-0.1680
1250	-0.06676	-0.24841	-0.1728	0.0131
1500	-0.17680	-0.21463	0.0247	0.0742
1750	-0.24884	-0.31322	0.1902	0.0535
2000	-0.30446	-0.27050	0.3667	-0.0527

Table 5.3: Equivalent potential temperature lapse rates ($\overline{d\theta_e/dz}$ (K/km)) in the the CTL and T50 simulations between 500 and 2500 meters. Each lapse rate was averaged over 0.25° longitude bins centered at 72°W, 71.5°W, and 71°W.

Equivalent Potential Temperature Lapse Rate ($\overline{d\theta_e/dz}$ (K/km))						
Time	00 UTC 01 Oct		03 UTC 01 Oct		06 UTC 01 Oct	
Longitude	CTL	T50	CTL	T50	CTL	T50
72°W	-4.97573	-3.79972	-3.14095	-6.60834	-5.28034	-7.32352
71.5°W	-7.02220	-4.64042	-4.00831	-4.58791	-2.76829	-4.59961
71°W	-4.51704	-4.75811	-3.14095	-4.83186	-5.28034	-6.18439

Chapter 6

Conclusion and Future Work

The primary focus of the study was to understand the characteristics of a persistent convective feature to the northeast of Hurricane Matthew's center, and explain the impact of terrain on this feature as well as the inner core structure. Elevated topography is known to create a drier atmospheric layer downstream (leeward) of the terrain through adiabatic downslope flow. The presence of a drier layer above an extremely moist surface layer produces a moist statically unstable environment conducive to convective initiation. Increased convection, including within the rainband of concern, may be favorable to TC intensification through improved warm core structure. To evaluate this hypothesis, a WRF-ARW model control simulation of Hurricane Matthew was created and then altered by reducing the terrain over northern South America.

As with any modeling study, shortcomings in the model and/or in the initial conditions can lead to challenges when trying to reproduce the observed TC. Intensity was difficult to replicate with both simulations failing to undergo rapid intensification (RI) as observed in Hurricane Matthew. However, in both simulations, the TC track followed a similar path to the observed and was far enough south for the TC wind field to interact with the elevated South American topography to test our hypothesis on the impact of remote terrain on TC structure. A weakening phase limited the time period over which the rainband could be analyzed before it dissipated, but the simulations still provided approximately 12 hours (between 21 UTC 30 September and 09 UTC 01 October) of valuable model output for this analysis.

For the first research question, I evaluated whether Hurricane Matthew's robust, persistent convective feature was associated with a principal rainband (PRB). When analyzing this rainband, convergence was found on the inner side of the rainband and inertial stability was greater than $2 \times 10^{-7} \text{ (s}^{-2}\text{)}$. These results match characteristics of inner core rainbands, and therefore, the rainband northeast of the TC center in the CTL simulation is consistent with previously defined characteristics of a PRB.

To address the second research question, I assessed the convection downstream of the northern South America terrain to evaluate whether the altered environment enhanced the convection within the rainband. When comparing the two simulation's PRBs, large differences in intensity were not apparent, as rainfall rates and reflectivity were similar to each other. The biggest difference occurred in the location of the PRB. Later on, the PRB seemed to dissipate faster in the T50 simulation as an outer core MCS developed. Spatially averaged skew-Ts near the convective initiation showed a significantly drier boundary layer in the CTL. Atmospheric layers downstream of terrain tend to be drier, which may have been due to adiabatic warming of downslope flow, leading evidence to support that the terrain played an important role in controlling moisture in this layer. As outlined in my hypothesis, the dry air overlying a very moist marine boundary layer could have led to increased moist static instability and aided in maintaining the PRB. Equivalent potential temperature lapse rates calculated in this area did not support the hypothesis, though statistically significant results were not found. Overall, based on these results, terrain did not factor into the peak rain rates in the rainband, but may have aided in the prolonged convection.

Lastly, differences in inner core structure between the CTL and T50 simulations were diagnosed to evaluate the third research question. Intensity time series plots did not

identify large differences between the CTL and T50 simulations. Although $MSLP_{min}$ was similar, discrepancies in intensity surfaced in the azimuthally averaged plots. The CTL simulation had a stronger RMW and warm core when compared to the T50 simulation. Also, the T50 simulation displayed a strong low-level outflow signature near the TC inner circulation, different from the CTL simulation which displayed strong low-level inflow approximately 40 kilometers away from the TC center. These results exhibit a structurally weaker TC in the T50 simulation. Further investigation is required to relate the differences in TC structure to the reduced topography in T50 simulation.

Although the results of this study provided interesting outcomes, further research needs to be conducted to develop a more robust cause-effect relationship between remote terrain and TC structure. First, an ensemble of the simulations would be necessary to rule out differences due to model and initial condition uncertainty. Second, I would like to calculate backtrajectories to identify the source regions of airstreams entering the PRB. Along with the backtrajectories, cross sections of thermodynamic variables following the airstreams would show temporal changes as the air mass moves over the terrain. Third, including more experimental simulations of various terrain height including 0%, 25%, and 150% would provide more data to explain the impact of terrain on TC structure. Lastly, I would like to evaluate these findings on other TCs to examine the impact of remote terrain on their TC structure. Incorporating the additional analyses outlined above would offer more insight beyond the results shown in Chapter 5 to reach a more thorough conclusion on the impact of remote terrain on TC structure.

SOURCES

- Arakawa, A., and V. R. Lamb, 1977: Computational Design of the Basic Dynamical Processes of the UCLA General Circulation Model. *Methods in Computational Physics: Advances in Research and Applications*, J. Chang, Ed., Vol. 17 of *General Circulation Models of the Atmosphere*, Elsevier, 173–265
<http://www.sciencedirect.com/science/article/pii/B9780124608177500094>
- Bender, M. A., 1997: The Effect of Relative Flow on the Asymmetric Structure in the Interior of Hurricanes. *J. Atmos. Sci.*, **54**, 703–724, doi:[10.1175/1520-0469\(1997\)054<0703:TEORFO>2.0.CO;2](https://doi.org/10.1175/1520-0469(1997)054<0703:TEORFO>2.0.CO;2).
- , R. E. Tuleya, and Y. Kurihara, 1987: A Numerical Study of the Effect of Island Terrain on Tropical Cyclones. *Mon. Wea. Rev.*, **115**, 130–155, doi:[10.1175/1520-0493\(1987\)115<0130:ANSOTE>2.0.CO;2](https://doi.org/10.1175/1520-0493(1987)115<0130:ANSOTE>2.0.CO;2).
- Braun, S. A., M. T. Montgomery, and Z. Pu, 2006: High-Resolution Simulation of Hurricane Bonnie (1998). Part I: The Organization of Eyewall Vertical Motion. *J. Atmos. Sci.*, **63**, 19–42, doi:[10.1175/JAS3598.1](https://doi.org/10.1175/JAS3598.1).
- Bryan, G. H., and R. Rotunno, 2009: The Maximum Intensity of Tropical Cyclones in Axisymmetric Numerical Model Simulations. *Mon. Wea. Rev.*, **137**, 1770–1789, doi:[10.1175/2008MWR2709.1](https://doi.org/10.1175/2008MWR2709.1).
- Cangialosi, J., 2018: *National Hurricane Center Forecast Verification*.
<https://www.nhc.noaa.gov/verification/verify5.shtml>
- Chen, B.-F., R. L. Elsberry, and C.-S. Lee, 2014: Origin and Maintenance of the Long-Lasting, Outer Mesoscale Convective System in Typhoon Fengshen (2008). *Monthly Weather Review; Washington*, **142**, 2838–2859.
- , ———, and ———, 2016: Synoptic controls of outer mesoscale convective systems with high impact rainfall in western north pacific tropical cyclones. *Asia-Pacific J Atmos Sci*, **52**, 11–23, doi:[10.1007/s13143-015-0085-2](https://doi.org/10.1007/s13143-015-0085-2).
- Corbosiero, K. L., and J. Molinari, 2002: The effects of vertical wind shear on the distribution of convection in tropical cyclones. *Monthly Weather Review; Washington*, **130**, 2110.
- , and ———, 2003: The relationship between storm motion, vertical wind shear, and convective asymmetries in tropical cyclones. *Journal of the Atmospheric Sciences; Boston*, **60**, 366–376.
- Davis, C., and L. F. Bosart, 2002: Numerical Simulations of the Genesis of Hurricane Diana (1984). Part II: Sensitivity of Track and Intensity Prediction. *Mon. Wea. Rev.*, **130**, 1100–1124, doi:[10.1175/1520-0493\(2002\)130<1100:NSOTGO>2.0.CO;2](https://doi.org/10.1175/1520-0493(2002)130<1100:NSOTGO>2.0.CO;2).
- , 2018: Resolving Tropical Cyclone Intensity in Models. *Geophysical Research Letters*, **45**, 2082–2087, doi:[10.1002/2017GL076966](https://doi.org/10.1002/2017GL076966).
- Emanuel, K. A., 1988: The Maximum Intensity of Hurricanes. *J. Atmos. Sci.*, **45**, 1143–1155, doi:[10.1175/1520-0469\(1988\)045<1143:TMIOH>2.0.CO;2](https://doi.org/10.1175/1520-0469(1988)045<1143:TMIOH>2.0.CO;2).
- , 1986: An Air-Sea Interaction Theory for Tropical Cyclones. Part I: Steady-State Maintenance. *J. Atmos. Sci.*, **43**, 585–605, doi:[10.1175/1520-0469\(1986\)043<0585:AASITF>2.0.CO;2](https://doi.org/10.1175/1520-0469(1986)043<0585:AASITF>2.0.CO;2).
- Euler, C., and C. Euler, 2018: Ventilation and Storm Structure during Extratropical Transition of Tropical Cyclones. 33rd Conference on Hurricanes and Tropical Meteorology, AMS <https://ams.confex.com/ams/33HURRICANE/webprogram/Paper340002.html> (Accessed January 2, 2019).

- Fierro, A. O., R. F. Rogers, F. D. Marks, and D. S. Nolan, 2009: The Impact of Horizontal Grid Spacing on the Microphysical and Kinematic Structures of Strong Tropical Cyclones Simulated with the WRF-ARW Model. *Mon. Wea. Rev.*, **137**, 3717–3743, doi:[10.1175/2009MWR2946.1](https://doi.org/10.1175/2009MWR2946.1).
- Frank, W. M., and E. A. Ritchie, 1999: Effects of environmental flow upon tropical cyclone structure. *Monthly Weather Review; Washington*, **127**, 2044.
- , and ———, 2001: Effects of vertical wind shear of the intensity and structure of numerically simulated hurricanes. *Monthly Weather Review; Washington*, **129**, 2249.
- Ge, X., T. Li, and M. Peng, 2013: Effects of Vertical Shears and Midlevel Dry Air on Tropical Cyclone Developments*. *Journal of the Atmospheric Sciences; Boston*, **70**, 3859–3875.
- Gentry, M. S., and G. M. Lackmann, 2009: Sensitivity of Simulated Tropical Cyclone Structure and Intensity to Horizontal Resolution. *Mon. Wea. Rev.*, **138**, 688–704, doi:[10.1175/2009MWR2976.1](https://doi.org/10.1175/2009MWR2976.1).
- Gray, W. M., 1968: Global view of the origin of tropical disturbances and storms. *Mon. Wea. Rev.*, **96**, 669–700, doi:[10.1175/1520-0493\(1968\)096<0669:GVOTOO>2.0.CO;2](https://doi.org/10.1175/1520-0493(1968)096<0669:GVOTOO>2.0.CO;2).
- Guinn, T. A., and W. H. Schubert, 1993: Hurricane Spiral Bands. *J. Atmos. Sci.*, **50**, 3380–3403, doi:[10.1175/1520-0469\(1993\)050<3380:HSB>2.0.CO;2](https://doi.org/10.1175/1520-0469(1993)050<3380:HSB>2.0.CO;2).
- Hence, D. A., and R. A. Houze, 2008: Kinematic structure of convective-scale elements in the rainbands of Hurricanes Katrina and Rita (2005). *Journal of Geophysical Research: Atmospheres*, **113**, doi:[10.1029/2007JD009429](https://doi.org/10.1029/2007JD009429).
<https://agupubs.onlinelibrary.wiley.com/doi/abs/10.1029/2007JD009429> (Accessed September 21, 2018).
- Houze, R. A., 2010: Clouds in Tropical Cyclones. *Monthly Weather Review; Washington*, **138**, 293-297,299-344.
- , 2012: Orographic effects on precipitating clouds. *Reviews of Geophysics; Washington*, **50**, doi:<http://dx.doi.org.ezproxy.lib.vt.edu/10.1029/2011RG000365>.
<https://search.proquest.com/docview/1026760764/abstract/48053FE52734076PQ/1> (Accessed October 24, 2017).
- , S. S. Chen, B. F. Smull, W.-C. Lee, and M. M. Bell, 2007: Hurricane Intensity and Eyewall Replacement. *Science*, **315**, 1235–1239, doi:[10.1126/science.1135650](https://doi.org/10.1126/science.1135650).
- Huffman, G. J., 2018: NASA Global Precipitation Measurement (GPM) Integrated Multi-satellitE Retrievals for GPM (IMERG)
https://pmm.nasa.gov/sites/default/files/document_files/IMERG_ATBD_V5.2_0.pdf
- Jiang, H., and E. M. Ramirez, 2013: Necessary Conditions for Tropical Cyclone Rapid Intensification as Derived from 11 Years of TRMM Data. *J. Climate*, **26**, 6459–6470, doi:[10.1175/JCLI-D-12-00432.1](https://doi.org/10.1175/JCLI-D-12-00432.1).
- , ———, and D. J. Cecil, 2012: Convective and Rainfall Properties of Tropical Cyclone Inner Cores and Rainbands from 11 Years of TRMM Data. *Mon. Wea. Rev.*, **141**, 431–450, doi:[10.1175/MWR-D-11-00360.1](https://doi.org/10.1175/MWR-D-11-00360.1).
- Johnson, D. H., 1962: METEOROLOGY. *Science Progress (1933-)*, **50**, 403–419.
- Jones, S. C., and Coauthors, 2003: The Extratropical Transition of Tropical Cyclones: Forecast Challenges, Current Understanding, and Future Directions. *Wea. Forecasting*, **18**, 1052–1092, doi:[10.1175/1520-0434\(2003\)018<1052:TETOTC>2.0.CO;2](https://doi.org/10.1175/1520-0434(2003)018<1052:TETOTC>2.0.CO;2).
- Kirshbaum, D. J., B. Adler, N. Kalthoff, C. Barthlott, and S. Serafin, 2018: Moist Orographic Convection: Physical Mechanisms and Links to Surface-Exchange Processes. *Atmosphere*, **9**, 80, doi:[10.3390/atmos9030080](https://doi.org/10.3390/atmos9030080).

- Kovacs, M., and D. J. Kirshbaum, 2016: Topographic Impacts on the Spatial Distribution of Deep Convection over Southern Quebec. *J. Appl. Meteor. Climatol.*, **55**, 743–762, doi:[10.1175/JAMC-D-15-0239.1](https://doi.org/10.1175/JAMC-D-15-0239.1).
- Li, X., and Z. Pu, 2008: Sensitivity of Numerical Simulation of Early Rapid Intensification of Hurricane Emily (2005) to Cloud Microphysical and Planetary Boundary Layer Parameterizations. *Mon. Wea. Rev.*, **136**, 4819–4838, doi:[10.1175/2008MWR2366.1](https://doi.org/10.1175/2008MWR2366.1).
- Laing, A., and J. L. Evans, 2015: *Introduction to tropical meteorology, 2nd Edition*. The COMET Program, http://www.meted.ucar.edu/tropical/textbook_2nd_edition/index.htm.
- Matyas, C. J., 2009: A Spatial Analysis of Radar Reflectivity Regions within Hurricane Charley (2004). *J. Appl. Meteor. Climatol.*, **48**, 130–142, doi:[10.1175/2008JAMC1910.1](https://doi.org/10.1175/2008JAMC1910.1).
- McNulty, R. P., 1995: Severe and Convective Weather: A Central Region Forecasting Challenge. *Wea. Forecasting*, **10**, 187–202, doi:[10.1175/1520-0434\(1995\)010<0187:SACWAC>2.0.CO;2](https://doi.org/10.1175/1520-0434(1995)010<0187:SACWAC>2.0.CO;2).
- Montgomery, M. T., and R. J. Kallenbach, 1997: A theory for vortex rossby-waves and its application to spiral bands and intensity changes in hurricanes. *Quarterly Journal of the Royal Meteorological Society*, **123**, 435–465, doi:[10.1002/qj.49712353810](https://doi.org/10.1002/qj.49712353810).
- Nolan, D. S., Y. Moon, and D. P. Stern, 2007: Tropical Cyclone Intensification from Asymmetric Convection: Energetics and Efficiency. *J. Atmos. Sci.*, **64**, 3377–3405, doi:[10.1175/JAS3988.1](https://doi.org/10.1175/JAS3988.1).
- Pasrez-Betancourt, D., 2011: Rapid intensification of Hurricane Earl in advanced hurricane WRF model simulations. <https://opensky.ucar.edu:islandora/object/manuscripts%3A638/> (Accessed March 25, 2019).
- Ramsay, H. A., and L. M. Leslie, 2008: The Effects of Complex Terrain on Severe Landfalling Tropical Cyclone Larry (2006) over Northeast Australia. *Mon. Wea. Rev.*, **136**, 4334–4354, doi:[10.1175/2008MWR2429.1](https://doi.org/10.1175/2008MWR2429.1).
- Reasor, P. D., M. T. Montgomery, and L. D. Grasso, 2004: A New Look at the Problem of Tropical Cyclones in Vertical Shear Flow: Vortex Resiliency. *J. Atmos. Sci.*, **61**, 3–22, doi:[10.1175/1520-0469\(2004\)061<0003:ANLATP>2.0.CO;2](https://doi.org/10.1175/1520-0469(2004)061<0003:ANLATP>2.0.CO;2).
- Riemer, M., 2016: Meso- β -scale environment for the stationary band complex of vertically sheared tropical cyclones. *Q.J.R. Meteorol. Soc.*, **142**, 2442–2451, doi:[10.1002/qj.2837](https://doi.org/10.1002/qj.2837).
- Schubert, W. H., and J. J. Hack, 1982: Inertial Stability and Tropical Cyclone Development. *J. Atmos. Sci.*, **39**, 1687–1697, doi:[10.1175/1520-0469\(1982\)039<1687:ISATCD>2.0.CO;2](https://doi.org/10.1175/1520-0469(1982)039<1687:ISATCD>2.0.CO;2).
- Stern, D. P., and D. S. Nolan, 2011: On the Height of the Warm Core in Tropical Cyclones. *J. Atmos. Sci.*, **69**, 1657–1680, doi:[10.1175/JAS-D-11-010.1](https://doi.org/10.1175/JAS-D-11-010.1).
- Stewart, S., 2017: *Hurricane Matthew*. National Hurricane Center, <https://www.nhc.noaa.gov/data/tcr/index.php?season=2016> (Accessed May 1, 2018).
- US Department of Commerce, N., 2018: ESRL : PSD : NOAA OI SST V2: High Resolution. <https://www.esrl.noaa.gov/psd/data/gridded/data.noaa.oisst.v2.highres.html#detail> (Accessed May 1, 2018).
- Wang, Y., and G. J. Holland, 1996: Tropical Cyclone Motion and Evolution in Vertical Shear. *J. Atmos. Sci.*, **53**, 3313–3332, doi:[10.1175/1520-0469\(1996\)053<3313:TCMAEI>2.0.CO;2](https://doi.org/10.1175/1520-0469(1996)053<3313:TCMAEI>2.0.CO;2).
- Wang, Y., and C.-C. Wu, 2004: Current understanding of tropical cyclone structure and intensity changes – a review. *Meteorol Atmos Phys*, **87**, 257–278, doi:[10.1007/s00703-003-0055-6](https://doi.org/10.1007/s00703-003-0055-6).

- Weatherford, C. L., and W. M. Gray, 1988: Typhoon Structure as Revealed by Aircraft Reconnaissance. Part I: Data Analysis and Climatology. *Mon. Wea. Rev.*, **116**, 1032–1043, doi:[10.1175/1520-0493\(1988\)116<1032:TSARBA>2.0.CO;2](https://doi.org/10.1175/1520-0493(1988)116<1032:TSARBA>2.0.CO;2).
- Wei-Jen Chang, S., 1982: The Orographic Effects Induced by an Island Mountain Range on Propagating Tropical Cyclones. *Mon. Wea. Rev.*, **110**, 1255–1270, doi:[10.1175/1520-0493\(1982\)110<1255:TOEIBA>2.0.CO;2](https://doi.org/10.1175/1520-0493(1982)110<1255:TOEIBA>2.0.CO;2).
- Willoughby, H. E., F. D. Marks, and R. J. Feinberg, 1984: Stationary and Moving Convective Bands in Hurricanes. *J. Atmos. Sci.*, **41**, 3189–3211, doi:[10.1175/1520-0469\(1984\)041<3189:SAMCBI>2.0.CO;2](https://doi.org/10.1175/1520-0469(1984)041<3189:SAMCBI>2.0.CO;2).
- , 1988: The dynamics of the tropical cyclone core. *Australian Meteorol. Mag.*, **36**, 183–191.

